

RESEARCH INTERNSHIP REPORT

Superfluidity of Light

Author:

Pauline BOUCHER
Promotion X2011
Ecole Polytechnique

Supervisor:

Pr. Quentin GLORIEUX

May 26, 2015 - August 16, 2015

Laboratoire Kastler Brossel

Université Pierre et Marie Curie

4 place Jussieu 75005 Paris

Abstract

Acknowledgements

Contents

Abstract	i
Acknowledgements	ii
Contents	iii
1 Theory overview	1
1.1 Bose-Einstein condensation	1
1.1.1 Bose-Einstein condensates	2
1.1.2 Superfluidity	3
1.2 Exciton-Polaritons	5
1.2.1 Polaritons	5
1.2.2 Excitons	5
1.2.3 Microcavity polaritons	6
1.3 The Quantum Optics group at Laboratoire Kastler Brossel	6
1.4 Quantum fluids of light in cavityless configurations	10
1.4.1 Theoretical description of light in a nonlinear media	10
1.4.2 Sound waves	11
1.4.3 Propagation on a defect	12
2 Experiment	15
2.1 “Experimental characterization of nonlocal photon fluids”	15
2.1.1 Theory overview	15
2.1.2 Photon fluid dispersion experiment	16
2.1.3 Pump and probe experiment	18
2.2 New experiment	18
2.2.1 Rubidium vapour as an optical nonlinear media	18
2.2.2 Imaging different propagation lengths	20
2.2.3 Implementation of the experiment	21
2.3 Laser source	22
2.3.1 Matisse Laser	22
2.3.2 SolsTiS® Laser	24
2.4 Saturated Absorption	25
2.4.1 Theory	25
2.4.2 Acousto-optic modulator	34
2.4.3 Experimental results	35

2.5	Laser locking	35
2.5.1	Heterodyne detection	35
2.5.2	PID controller	38
2.6	Photon fluid experiment	38

Bibliography

41

Chapter 1

Theory overview

1.1 Bose-Einstein condensation

Quantum physics distinguishes two categories of particle: bosons, which have a symmetric wavefunction for the exchange of two particles, and fermions, which have an antisymmetric wavefunction under this action. These two kinds of particles follow different statistics. Fermions follow the Fermi-Dirac distribution:

$$n_i^F = \frac{g_i}{\exp\left(\frac{E_i - \mu}{k_B T}\right) + 1} \quad (1.1)$$

while bosons follow the Bose-Einstein distribution:

$$n_i^B = \frac{g_i}{\exp\left(\frac{E_i - \mu}{k_B T}\right) - 1}. \quad (1.2)$$

where n_i is the number of particles at the energy level E_i , g_i is the the degeneracy of energy level E_i , μ is the chemical potential, k_B is the Boltzmann constant and T is the temperature.

1.1.1 Bose-Einstein condensates

At thermodynamical equilibrium and at low temperature, identical bosons which do not interact one with another, should condensate into the ground energy level and become indiscernable. This phenomenon is known as Bose-Einstein condensation.

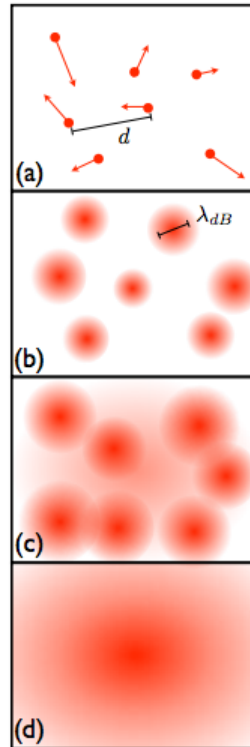


FIGURE 1.1: Transition of a boson gas between the classical high temperature representation, to the Bose-Einstein condensate. Taken from [1].

Figure 1.1 shows the evolution of a boson gas at high temperature towards a Bose-Einstein condensate. At high temperature, we can describe the particles in a classical fashion (figure 1.1 (a)). The speed of a particle is described by a vector, and d is the average distance between two particles. As the temperature decreases (figure 1.1 (b)), particles can no longer be described classically. They are described by their thermal de Broglie wavelength λ_{dB} which is given by:

$$\lambda_{dB} = \sqrt{\frac{2\pi\hbar^2}{mk_B T}}. \quad (1.3)$$

As the temperature decreases, λ_{dB} becomes of the order of d and the wavepackets start to overlap. Part of the gas is said to condensate and can be described by a macroscopic wavefunction. Finally, at $T = 0$ K, the gas is completely condensated (figure 1.1 (d)). The first experimental observation of Bose-Einstein condensation was made by M. H.

Anderson et al.[2] in a dilute rubidium vapour. The dilution was necessary to neglect the interactions between atoms and allow condensation. However, these interactions still play a role and must be taken into account when describing the different characteristics of such systems.

In the mean field approximation, a N particle condensate can be described with the following wavefunction: $\hat{\Phi}(\mathbf{x}_1, \mathbf{x}_2, \dots, \mathbf{x}_N) = \Pi_N \hat{\Psi}_i(\mathbf{r}_i)$. $\hat{\Psi}_i$ is the wavefunction of one particle and $\int |\hat{\Psi}|^2 d\mathbf{x} = N$. With the pseudopotential model, L. P. Pitaevskii [3] and E. P. Gross [4] have shown that the evolution of the wavefunction could be described by what is known as the Gross-Pitaevskii equation or nonlinear Schrödinger equation:

$$i\hbar \frac{\partial \hat{\Psi}(\mathbf{x})}{\partial t} = \left(-\frac{\hbar^2}{2m} \nabla^2 + V(\mathbf{x}) + g|\hat{\Psi}(\mathbf{x})|^2 \right) \hat{\Psi}(\mathbf{x}). \quad (1.4)$$

m is the mass of the particles, V is a potential and g is the coupling constant such that $g = 4\pi\hbar^2 a_s/m$ where a_s is the diffusion length between the particles.

1.1.2 Superfluidity

Superfluidity was discovered in 1937 by P. Kapitza, J.F. Allen et D. Missener with Helium 4 [5, 6]. This phenomenon was explained in 1941 by Landau [7].

Landau criterion

[8] Let us consider a fluid, at zero Kelvin, which flows into a tube with a constant speed \mathbf{v} . In a referential moving at \mathbf{v} , where the fluid is at rest, if an excitation of impulsion \mathbf{p} appears, the energy becomes $E_0 + \epsilon(\mathbf{p})$ with E_0 the fundamental energy level and $\epsilon(\mathbf{p})$ the energy of the excitation. In the referential of the tube, the energy E' and the impulsion \mathbf{P}' are given by:

$$\begin{aligned} E' &= E_0 + \epsilon(\mathbf{p}) + \mathbf{p} \cdot \mathbf{v} + \frac{1}{2} M v^2 \\ \mathbf{P}' &= \mathbf{p} + M \mathbf{v} \end{aligned} \quad (1.5)$$

where M is the mass of the fluid. $\epsilon(\mathbf{p}) + \mathbf{p} \cdot \mathbf{v}$ is the energy of an elementary excitation in the referential of the tube. Elementary excitations can only spontaneously appear if their contribution to the energy of the system is negative:

$$\epsilon(\mathbf{p}) + \mathbf{p} \cdot \mathbf{v} < 0. \quad (1.6)$$

This criterion is satisfied for $v > \epsilon(\mathbf{p})/|\mathbf{p}|$: in this case, the fluid is unstable, excitations are generated spontaneously and the viscosity is non zero. On the contrary, if the speed of the fluid is smaller than v_c where :

$$v_c = \min_{\mathbf{p}} \frac{\epsilon(\mathbf{p})}{p} \quad (1.7)$$

equation 1.6 is never true and no excitation can be spontaneously generated. The Landau criterion states that if the fluid speed is smaller than the critical velocity v_c , the fluid's flow will be frictionless.

Elementary excitations

For an interaction Bose-Einstein condensate without potential, we can use the Gross-Pitaevskii equation (1.4). We will consider a small perturbation of impulsion $\mathbf{p} = \hbar\mathbf{k}$ and a condensate with a stationary wavefunction Φ_0 and density n_0 . The perturbed wavefunction undergoes a Bogoliubov transformation and is given by:

$$\Psi(\mathbf{r}, t) = \left(\Phi_0(\mathbf{r}) + A \exp^{i(\mathbf{k} \cdot \mathbf{r} - \omega t)} + B \exp^{-i(\mathbf{k} \cdot \mathbf{r} - \omega t)} \right) \exp^{-i\mu t/\hbar}. \quad (1.8)$$

Using this expression in the Gross-Pitaevskii equation (1.4), we get the following coupled equations:

$$\begin{aligned} \hbar\omega A &= \left(\frac{\hbar^2 k^2}{2m} - \mu + 2gn_0 \right) A + gn_0 B \\ -\hbar\omega B &= \left(\frac{\hbar^2 k^2}{2m} - \mu + 2gn_0 \right) B + gn_0 A \end{aligned} \quad (1.9)$$

For a uniform gas, $\mu = gn_0$. This coupled equation system can be solved if the corresponding matrix determinant is null, which translates into:

$$\hbar\omega_{\pm} = \pm \sqrt{\left(\frac{\hbar^2 k^2}{2m} \right)^2 + \frac{\hbar^2 k^2}{m} gn_0} \quad (1.10)$$

For small wave vectors, this allows to define a condensate speed of light:

$$c_s = \sqrt{\frac{gn_0}{m}}. \quad (1.11)$$

In this case, the critical speed from Landau criterion is the same as this sound velocity. According to the Landau criterion, a condensate possessing these characteristics will exhibit superfluidity for speeds inferior to c_s .

In the opposite case, the Bogoliubov dispersion law 1.10 becomes:

$$\hbar\omega = \frac{\hbar^2 k^2}{2m} + gn_0. \quad (1.12)$$

The transition between the two regimes takes place around the point where $\frac{\hbar^2 k^2}{2m} = gn_0$. We can define $\xi = 1/k$, the *healing length* such that:

$$\xi = \sqrt{\frac{\hbar^2}{2mgn_0}}. \quad (1.13)$$

1.2 Exciton-Polaritons

1.2.1 Polaritons

Polaritons are quasiparticles which are the result of the strong interaction between an electric or magnetic dipole transition and an electromagnetic field. If the transition and the electromagnetic mode have the same energy, and if their dispersion in energy is small enough, the energy levels of photons and those of the transition will experience a lifting of degeneracy. The emitter (the transition) and the emitted light (mode of the electromagnetic field) will hybridate. The two resulting modes can be seen as pseudo-particles which are called polaritons. Two kinds of polaritons appear: upper polaritons and lower polaritons. The energy gap between those two levels is called the Rabi shift and defines the Rabi frequency.

1.2.2 Excitons

In a crystal, the periodicity of the crystalline pattern introduces a band gap for the electrons. In a semi-conductor material, this gap stands between the conduction and valence bands. At low temperature, the valence band is the only one which is occupied. An optical excitation can cause one electron to be promoted to the conduction band,

leaving behind a “hole” in the valence band. This hole is a quasi-particle of positive charge, which can form a bound with the electron of the valence band. The composite quasi-particle, although made of two fermions, is a boson - an exciton.

Excitons are easily generated by using a laser source with an energy greater than the bandgap. The effective mass of the excitons is of the order of the mass of the free electron. As a consequence, their de Broglie wavelength is sufficiently large at 1 K to fulfill the Bose-Einstein condensation criterion. On the other hand, excitons have a very short lifetime: of the order of the picosecond.

1.2.3 Microcavity polaritons

In a semiconductor microcavity, the quantum well structure generates an exciton, while the cavity structure selects one mode of the electromagnetic field and enhances the coupling between the transition and the field. Microcavity polaritons result of the strong coupling between photons confined in a micro-cavity and excitons created in the quantum wells that lie within the microcavity. Those quasi-particles were first observed in 1992 by Weisbuch et al. [9]. Their energy levels form an upper and a lower branch.

A laser at high energy acts as an excitation. Excitons created will relax towards the bottom of the lower polariton branch, losing energy through acoustic or optical phonon interaction or polariton scattering. The radiative recombination process is a useful tool since the monitoring of the emitted photons provides information about the system: their angle of emission θ is related to their in-plane wavevector $k_{inplane}$ such that:

$$k_{inplane} = (E/\hbar c) \sin(\theta). \quad (1.14)$$

Kasprzak et al. [10], have demonstrated first the Bose-Einstein condensation of polaritons, at relatively high temperature (19 K).

1.3 The Quantum Optics group at Laboratoire Kastler Brossel

The team of Alberto Bramati, Elisabeth Giacobino and Quentin Glorieux in the Quantum Optics group of Laboratoire Kastler Brossel focuses on two main topics: nanophotonics and quantum fluids of light.

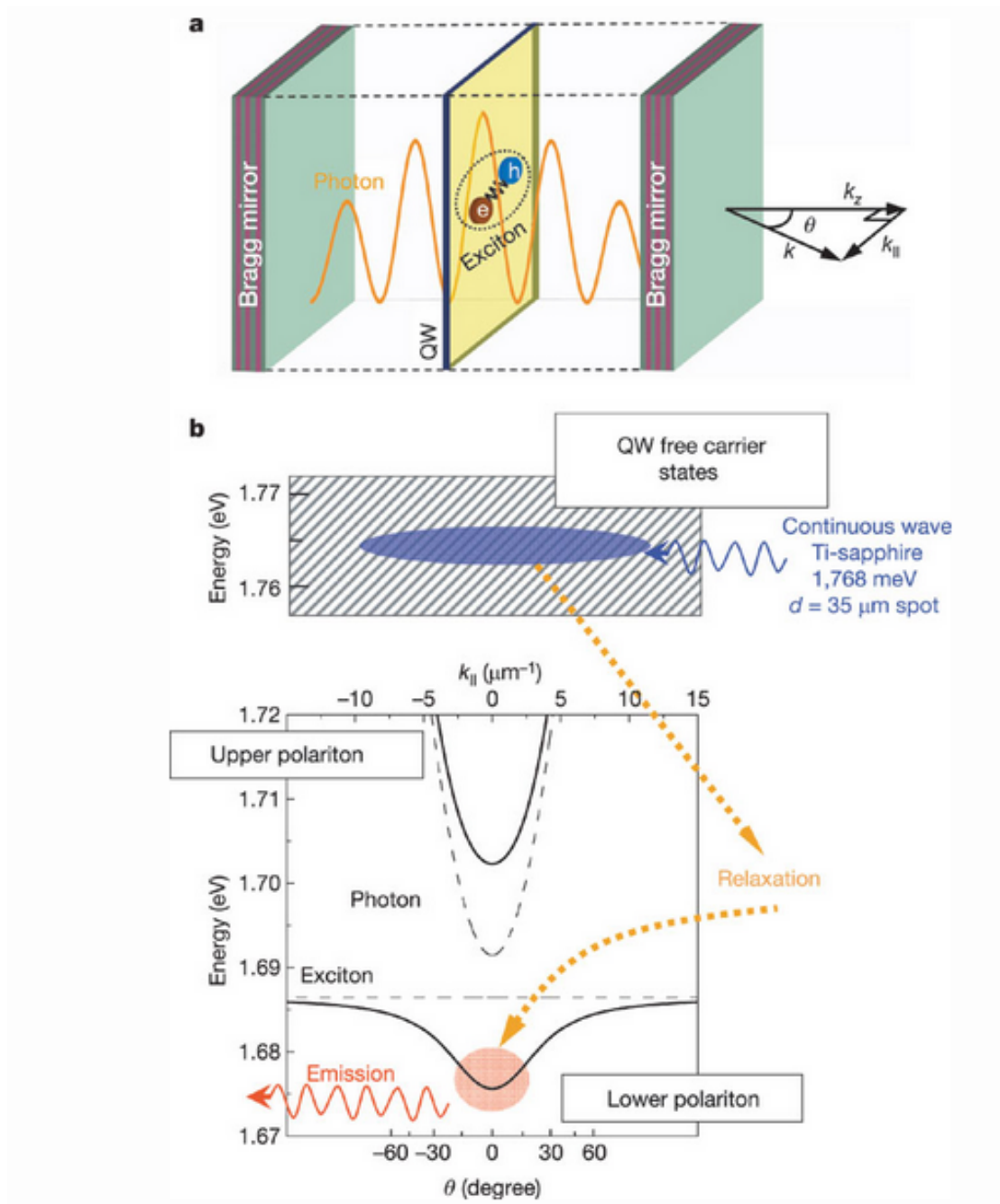


FIGURE 1.2: (a) A microcavity consists of two mirrors forming a Fabry-Pérot resonator. The mirrors are Bragg mirrors. Between the mirrors lie quantum wells in which excitons can form. In the strong coupling regime the excitons and the optical field will define new eigenmodes called microcavity polaritons. (b) Energy levels versus angle between the in-plane wavevector. Image and text from [10].

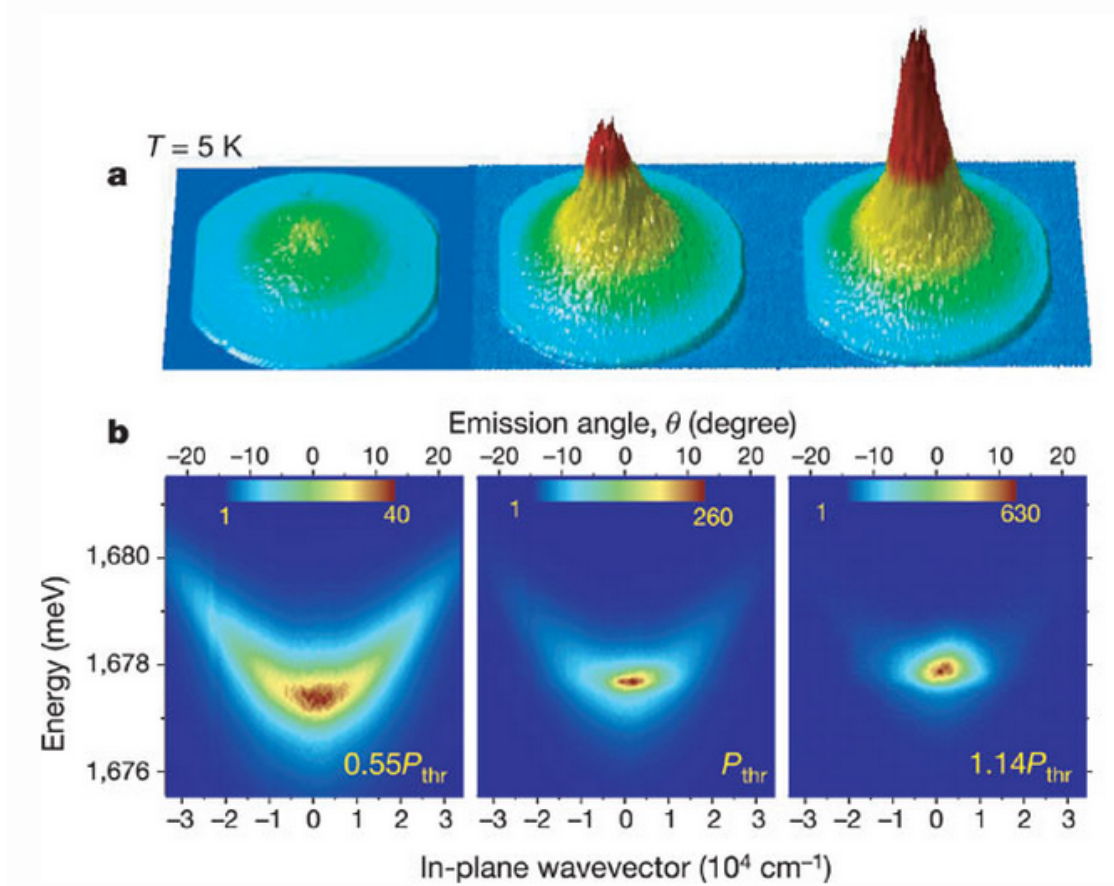


FIGURE 1.3: “Left panels, $0.55 P_{thr}$; centre panels, P_{thr} ; and right panels, $1.14 P_{thr}$; where $P_{thr} = 1.67 \text{ kW cm}^{-2}$ is the threshold power of condensation.” (a) Far field emission. As the power is increased, we observe a sharp rise of the intensity at $\theta_x = \theta_y = 0$ which corresponds to $k_{inplane} = 0$. (b) “Same data as (a) but resolved in energy.” Image and text from [10].

In order to study quantum fluids of light, two main supports are used: microcavity polaritons and atomic vapours near a resonance.

The superfluidity of a polaritonic fluid has been demonstrated in [11]. A polariton fluid is created by a laser with a given momentum in the plane of the microcavity. The defects, whether defects in the microcavity or controlled perturbations, are potential barriers for the polariton fluid. The modification of the laser power allows to navigate between the normal fluid and superfluid regimes. The authors were able to observe of a Cerenkov cone in the case where the fluid speed is superior to the speed of sound in the fluid. These observations are in good agreement with the Gross-Pitaevskii theory. Polaritons thus prove themselves to be a convenient tool to study out-of-equilibrium quantum fluids. Other topological excitations have been experimentally observed such as solitons and vortices [12–14].

Microcavity polariton also exhibit interesting polariton spin properties. In the linear

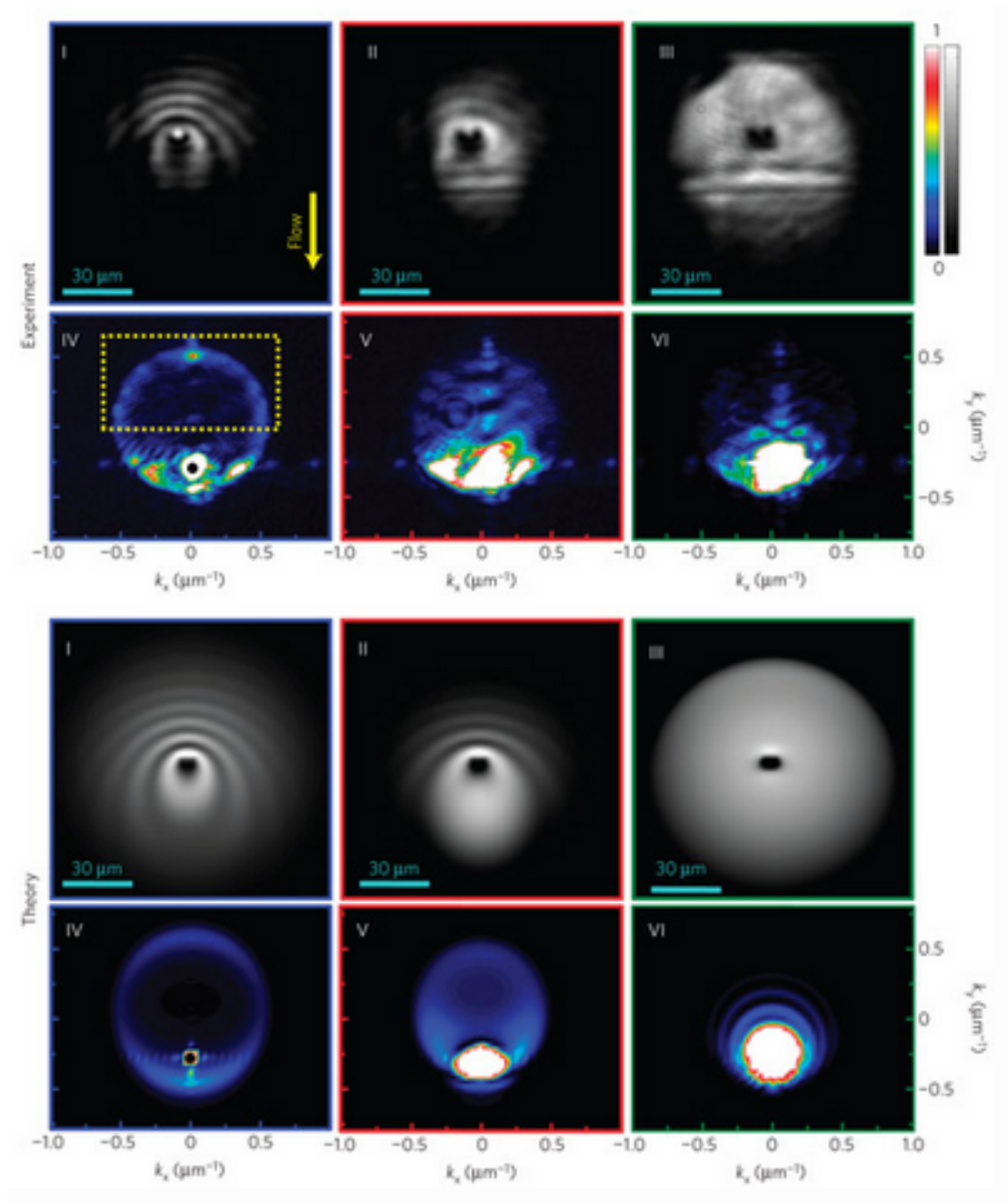


FIGURE 1.4: Observation of a polariton fluid. The top panels correspond to observations and the bottom panels correspond to calculations. Panels I to III correspond to the near-field while panels IV to VI correspond to far-field images. At low intensity, the scattering caused by the defect is responsible for the parabolic shaped fringes (I) and the ring shaped elastic scattering in far-field observations. As power increases (II-V), the interaction between polaritons become more important. At high power (III-VI), we have entered the superfluidity regime: no interference fringes can be observed and the elastic scattering ring in momentum space has disappeared.

regime, the dynamic of the polariton spin is similar to the Hall spin effect. The experimental demonstration of the transport of spin currents over large distances (of the order of 100 μm) was realized in the group [15, 16]. In the nonlinear regime, the polariton-polariton possesses “giant” nonlinearities. In this regime, experimental realization of a logical gate and an all-optical spin switch was made [17–19].

1.4 Quantum fluids of light in cavityless configurations

The $\chi(3)$ optical nonlinearity of an optical medium can be interpreted as the medium mediation of a photon-photon interaction. In such a media, a beam of light can be analyzed as a *quantum fluid of light* as opposed to a gas of non-interacting photons which is the classical description [20].

In [21] and [22], P.-E. Larré and I. Carusotto detail a theoretical frame which allows the description of the quantum dynamics of a fluid of light propagating in a bulk nonlinear medium without a cavity. We will in this part present this approach following the structure of [22].

1.4.1 Theoretical description of light in a nonlinear media

We consider a monochromatic beam at frequency ω_0 propagating in a nonlinear optical media characterized by a Kerr nonlinearity $\chi^{(3)}$. The propagation axis is designated as z and (x, y) is the transverse plane.

Light propagation is described by the nonlinear wave equation:

$$\partial_z^2 E(\mathbf{r}, z) + \nabla_{\perp}^2 E(\mathbf{r}, z) + \frac{\omega_0^2}{c^2} \left(\epsilon + \delta\epsilon(\mathbf{r}, z) + \chi^{(3)} |E(\mathbf{r}, z)|^2 \right) E(\mathbf{r}, z). \quad (1.15)$$

$\mathbf{r} = (x, y)$ and ϵ is the medium linear dielectric constant.

We assume that $\delta\epsilon(\mathbf{r}, z)$, the variation of the medium dielectric constant, varies slowly in space. We place ourselves in the paraxial approximation: $E(\mathbf{r}, z)$ is supposed to vary slowly in the transverse direction. This approximation is correct if $|\nabla_{\perp}^2 \mathcal{E}|/k_0^2 \simeq |\partial_z \mathcal{E}|/k_0 \ll 1$. Under this approximation, we write $\mathcal{E}(\mathbf{r}, z) = E(\mathbf{r}, z) \exp^{-ik_0 z}$ and the second derivative of \mathcal{E} with respect to z can be neglected. Equation 1.15 can be rewritten as a nonlinear Schrödinger equation:

$$i\partial_z \mathcal{E}(\mathbf{r}, z) = -\frac{1}{2k_0} \nabla_{\perp}^2 \mathcal{E} - \frac{k_0}{2\epsilon} \left(\delta\epsilon(\mathbf{r}, z) + \chi^{(3)} |\mathcal{E}(\mathbf{r}, z)|^2 \right) \mathbf{r}, \ddagger \quad (1.16)$$

The modulation of the dielectric constant can be interpreted as an external potential: $V(\mathbf{r}, z) = -\frac{k_0 \delta\epsilon(\mathbf{r}, z)}{2\epsilon}$. The optical nonlinearity can be interpreted as a photon-photon interaction constant: $g = -\frac{\chi^{(3)} k_0}{2}$.

The amplitude profile of the incident field as it hits the nonlinear medium gives the initial condition for $\mathcal{E}(\mathbf{r}, z = 0)$. If the incident plane wave direction defines an angle ϕ with respect to the propagation axis z , momentum conservation states that $k_{\perp}^{inc} = (\omega_0/c) \sin \phi$. The transverse flow speed is defined, in the paraxial approximation as:

$$v = \epsilon^{-1/2} \sin \phi \simeq \epsilon^{-1/2} \phi. \quad (1.17)$$

The term ‘‘fluid of light’’ as well as the hydrodynamical description of the evolution of the transverse beam profile comes from the similarity between equation 1.16 and the macroscopic wavefunction of a Bose-Einstein condensate (cf. equation ??).

The main difference between the two equations is that while the Gross-Pitaevskii equation describes the propagation of a Bose-Einstein condensate in time, equation 1.16 describes the evolution of the transverse beam profile in space. A space-time mapping is thus underlined when we speak of the evolution of a fluid of light.

1.4.2 Sound waves

The Bogoliubov theory of weak perturbations can be applied to a weakly interacting Bose-Condensate. We will here apply it in the fluid of light context. The dispersion of the elementary excitations on top of a uniform fluid of light of density $|E_0|^2$ at rest is given by:

$$W_{Bog}(\mathbf{k}_{\perp}) = \sqrt{\frac{k_{\perp}^2}{2k_0} \left(\frac{k_{\perp}^2}{2k_0} - \frac{k_0 \chi^{(3)} |E_0|^2}{\epsilon} \right)} \quad (1.18)$$

and the healing length has the following expression:

$$\xi = \left(-\frac{2\epsilon}{\chi^{(3)}|E_0|^2} \right)^{1/2} k_0^{-1}. \quad (1.19)$$

Finally, the speed of sound is given by:

$$c_s = \left(-\frac{\chi^{(3)}|E_0|^2}{2\epsilon} \right)^{1/2}. \quad (1.20)$$

The healing length separates two different regimes: small momentum excitations $k_\perp \xi \ll 1$ and large momentum excitations $k_\perp \xi \gg 1$. In the first case, the dispersion is given by $W_{Bog} \simeq c_s |\mathbf{k}|$. In this case, the excitations can be described as phonon waves propagating on top of the light fluid at the speed c_s . In the second case, the dispersion is given by $W_{Bog} \simeq k_\perp^2 / (2k_0)$. The excitations can be described individually as photons which are excited out of the condensated cloud to a high-momentum \mathbf{k}_\perp . Finally, in the limit of weak intensity, which corresponds to the classical optic case, we have $c_s \rightarrow 0$ and $\xi \rightarrow \infty$: all excitations are described as single-particles. We can note that this interpretation only holds for $\chi^{(3)} \neq 0$, since for $\chi^{(3)} = 0$, W_{Bog} becomes imaginary for small k_\perp : this phenomenon is known as the filamentation of a laser beam.

The authors propose the following experiment to observe the Bogoliubov modes. Two laser beams are used: a strong pump beams which creates the uniform background fluid of light and a weak probe beam which will be responsible for the creation of small excitations on top of the fluid of light. Control on the incidence angle of the probe beam ϕ_{pr} allows to control the in-plane wave vector of the excitation through $k_\perp^{pr} = (\omega_0/c) \sin \phi_{pr}$. By changing the intensity of the pump beam (i.e. $|E_0|^2$), one varies the healing length. This allows, for a fixed pump/probe configuration, to navigate between the two dispersion regimes: sonic and parabolic. Figure 1.5 illustrate the propagation of weak excitations in the collective excitation and particle-like regimes.

1.4.3 Propagation on a defect

In the superfluidity regime, a defect present in the path of the superfluid experiences no drag force. The situation studied here is that of a superfluid of light propagating at a finite speed and hitting a cylindrical defect. We describe this defect as a Gaussian-shaped modulation of the linear dielectric constant:

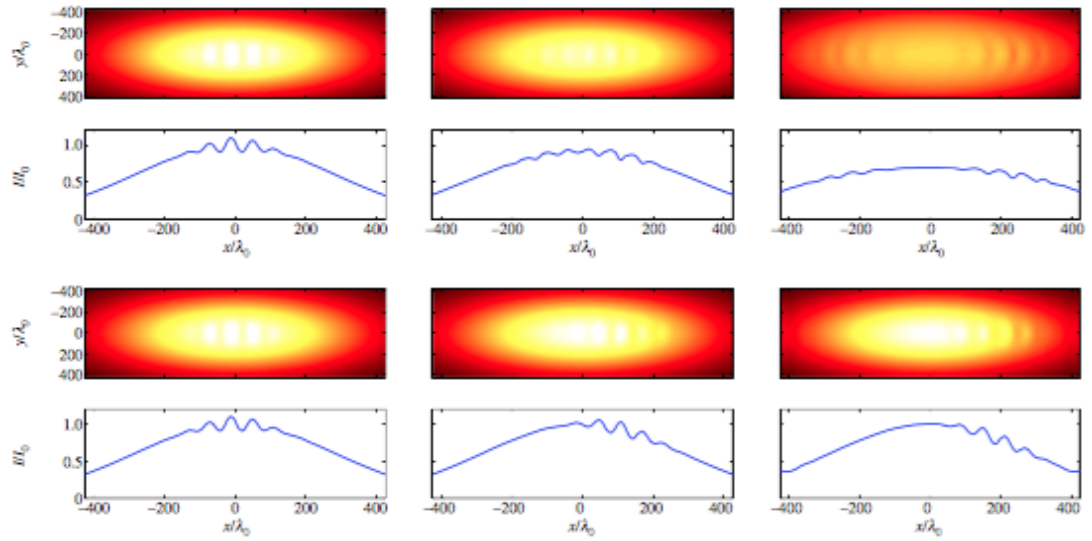


FIGURE 1.5: Propagation of excitations on top of a photon fluid. The pump and probe beams have Gaussian profiles, and a width ratio of 1/4. The upper row shows the propagation of an excitation in the collective excitation regime (snapshots at $z/\lambda_0 = 0, 3000$ and 7000) while the lower row shows its propagation in the single particle regime (snapshots at $z/\lambda_0 = 0, 7000$ and 12000). The transition between the two excitation regimes was made by changing the pump intensity. Taken from [22].

$$\delta\epsilon(\mathbf{r}_\perp, z) = \delta\epsilon_{max} \exp\left(-\frac{r_\perp^2}{2\sigma^2}\right) \quad (1.21)$$

for a defect centered on $\mathbf{r}_\perp = 0$ and of width σ .

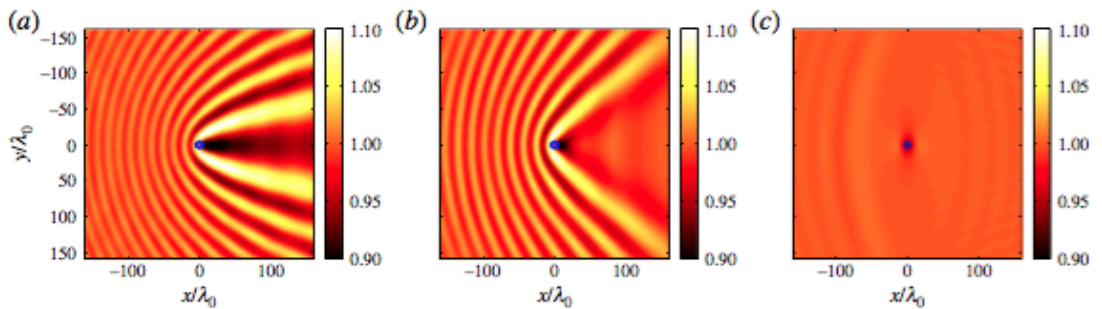


FIGURE 1.6: “Long-distance asymptotic transverse profiles of the laser beam intensity hitting a cylindrical defect located at $\mathbf{r}_\perp = 0$. The flow velocity is the same $v=0.034$ along the positive x -direction (rightward in the figure), while the light intensity is different in the three panels, increasing from left to right. The ∞ (linear optics limit, panel (a)), $v/c_s^0 = 1.84$ (supersonic flow regime, panel (b)) and $v/c_s^0 = 0.86$ (superfluid regime, panel (c)). [...]” [22].

Figure 1.6 presents the flow of the fluid of light on this defect. The incidence angle of the laser beam is kept constant while its intensity is increased in order to investigate the different propagation regimes. Figure 1.6(a) shows the linear optics case: the incoming and scattered light interfere, drawing parabolic shaped fringes. In figure 1.6(b), we are in the supersonic flow regime. We can observe the apparition of parabolic-like fringes upstream of the defects, but most importantly, we observe a Mach-Cerenkov cone downstream of the defect. The angular aperture of this cone is given by $\sin \theta = c_s^0/v$. Finally, figure 1.6(c) shows the superfluid case where the fluid possesses a subsonic speed. The nonlinearity suppresses the scattering of light by the defect. In [23], the authors show that this suppressed scattering is linked to the suppression of the radiation pressure acting on the defect.

Chapter 2

Experiment

2.1 “Experimental characterization of nonlocal photon fluids”

In this section we will present the experiment conducted by David Vocke et al., “Experimental characterization of nonlocal photon fluids” which we aimed at reproducing [24].

In the frame of quantum fluids of light, a powerful laser beam is studied as a gas in which the photons interact through the optical nonlinearity of the medium [20].

The “fluid” properties of such a system can easily be controlled through the phase and intensity of the optical field, the shape of the propagation medium or its index profile [25]. The optical nonlinearity which allows the photon-photon interaction is the third order Kerr non linearity which is characterized by $\Delta n = n_2|E|^2$. In order to have a dynamically stable photon fluid, the nonlinearity coefficient n_2 must be negative. In this experiment, this strong nonlinearity is obtained through the thermo-optic effect. The strong optical field used as a fluid of light will heat the medium in which it propagates, leading to a decrease in the refractive index. The change is proportional to the intensity of the laser field. This constitutes a repulsive photon-photon interaction.

2.1.1 Theory overview

The nonlinear Schrödinger equation describes the propagation of a laser beam through a nonlinear media:

$$\partial_z E = \frac{i}{2k} \nabla^2 E - \frac{ikn_2|E|^2}{n_0} E. \quad (2.1)$$

In our case, $n_2 < 0$ since we are in a self-defocusing media. If we write the field E as $E = E_{bg} \exp i\Phi$, equation 2.1 becomes:

$$\begin{aligned} \partial_\tau \rho + \nabla(\rho \mathbf{v}) &= 0 \\ \partial_\tau \Psi + \frac{1}{2}v^2 + \frac{c^2 n_2}{n_0^3} \rho - \frac{c^2}{2k^2 n_0^2} \frac{\nabla^2 \sqrt{\rho}}{\sqrt{\rho}} &= 0 \end{aligned} \quad (2.2)$$

where $\tau = zn_0/c$, $|E_{bg}|^2$ the background intensity is identified as the photon density ρ and the fluid velocity is defined with the optical phase as $\mathbf{v} = \left(\frac{c}{kn_0}\right) \nabla \Phi = \nabla \Psi$. In this form, these equations formally identify with the 2D equations for a Bose Einstein condensate (density and phase equations). In the regime of small amplitude perturbations ($E = E_{bg} + \epsilon$), the Bogoliubov theory can be applied to our system and allows the description of the perturbations in terms of sound waves on top of the photon fluid [22]. With this formalism, a sound mode possesses a wave vector \mathbf{K} and an angular frequency Ω such that:

$$(\omega - \mathbf{v}\mathbf{K})^2 = \frac{c^2 n_2 |E_{bg}|^2}{n_0^3} K^2 + \frac{c^2}{4k^2 n_0^2} K^4 \quad (2.3)$$

where c has its usual meaning and \mathbf{v} is the background flow velocity. Two regimes can be distinguished. For low frequencies, $\Omega \propto K$ and for high frequencies, $\Omega \propto K^2$. They are separated by a characteristic length, usually called the *healing length* for Bose Einstein condensates and which is written as $\xi = \lambda/2\sqrt{n_0|n_2||E_{bg}|^2}$. Using optics vocabulary, $K = \sqrt{K_x^2 + K_y^2}$ is the magnitude of the transverse wave vector and $\Omega = (c/n_0) \Delta K_z$ is linked to the variation of the the wave vector in the propagation direction.

The nonlinear medium chosen in this experiment is a methanol/graphene solution. Methanol has a negative thermo-optic coefficient but absorbs very little light. To counter this effect, nanometric graphene flakes were dissolved in the medium to increase the absorption coefficient of the medium. The concentration of graphene flakes was chosen for the sample to have 20 % absorption. The particularity of thermo-optical medium is that, since the nonlinear effect is linked to a heating of the medium, it is a highly non-local process. The authors have taken this particularity into account, which complexifies the form of the Bogoliubov dispersion relation.

2.1.2 Photon fluid dispersion experiment

The first experiment the authors implemented used the fact that in the situation studied, the z axis formally corresponds to the time coordinate. By measuring the profile of the laser beam at different distances in the sample, one can measure the evolution of the intensity fluctuations on top of the beam.

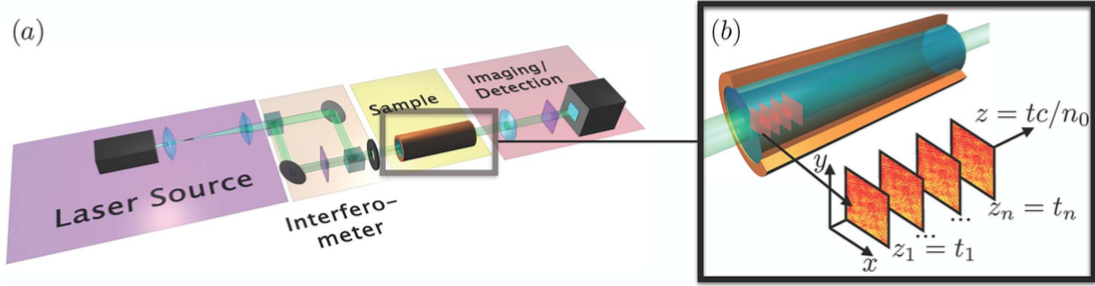


FIGURE 2.1: “(a) Experimental layout used for measuring the dispersion relation. A collimated, flat beam is launched through a cylindrical sample filled with a methanol/graphene solution and is imaged by a camera/lens system that can be translated along the propagation direction of the beam. (b) Detail of nonlinear sample showing example beam profiles at different propagation distances (i.e., equivalently for different propagation times) as measured in the experiment. An interferometer placed before the sample generates a pump and probe beam with a controllable relative angle (i.e., wavelength of the photon fluid excitations).” [24]

Surface waves naturally occur on top of the beam. The profile of the beam was recorded in both space and time. The Fourier transform of these measurements gives the dispersion relation of the medium.

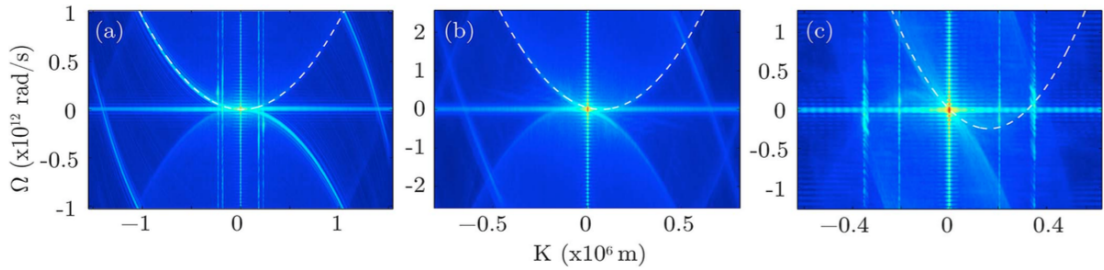


FIGURE 2.2: “Photon fluid dispersion relation with scanning distances of (a) 1.5 cm, (b) 5 cm and (c) 12 cm. The flow v of the effective medium can be controlled by the phase of the background field: (a) $v_{bg}=0$ m/s, (b) $v_{bg} = 1.3 \times 10^6$ m/s and (c) $v_{bg} = 3.0 \times 10^6$ m/s.” [24]

The large signal at $K = 0, \Omega = 0$ is due to the intense pump beam. The horizontal or vertical features are due to defects of the sample. Figures a), b) and c) correspond to three different angles of the input beam with respect to the sample. This tilt controls the transverse flow of the photon fluid. The main result is that we can observe what appears to be a purely parabolic dispersion relation for all K . However, since the imaging is done in a nonlinear media, the nonlinearity may lead to deformations of the recorded object planes. The authors have performed side measurements in order to verify that this does not falsify the results. The experimental results provide an excellent match to the theoretical model for $v_{bg} = 0$ and a good match for $v_{bg} > 0$.

2.1.3 Pump and probe experiment

The second experiment the authors carried out was a pump and probe experiment as proposed in [22]. A laser beam goes through a beam splitter producing the “pump” and “probe” beams. The probe beam is attenuated and tilted before being recombined with the pump beam. The interferometer thus created can be controlled in order to vary the modulation depth. The angle between the two beams controls the relative wave vector K . The photon fluid sound wave results in an interference pattern which is recorded at the output of the sample. The shift of this pattern in the x direction is measured as a function of the laser power. The measurements were made for several wavelengths $\Lambda = 2\pi/K$ with a constant power of 28 mW ($1\text{W}/\text{cm}^2$).

For $\Lambda > 0.7\text{mm}$, the shift appears to saturate which means that the dispersion relation is dominated by the linear Bogoliubov term. This is a proof of the collective excitation which characterizes a superfluid.

In conclusion, the authors have implemented an experiment characterizing the physics of a photon fluid, outside a cavity and at room temperature.

2.2 New experiment

The goal of this project was to reproduce the experiment of Vocke et al. [24] but using a different nonlinear medium. Indeed, as what was exposed in the previous part, the optical nonlinear medium used is highly non-local which complexifies theoretical and experimental results. Instead of using a methanol/graphene solution as the nonlinear medium needed to obtain a third order nonlinearity, we proposed to use Rubidium vapour.

2.2.1 Rubidium vapour as an optical nonlinear media

The use of atomic vapour as a nonlinear media has a long history [27, 28]. For the observation of nonlinear processes, resonant atomic media offers several advantages: due to the resonant enhancement of the interaction, nonlinear effects appear at low intensities. Moreover, the intensity of the nonlinear contribution can be tuned by adjusting the laser frequency closer or further away from the optical transition frequency. In the same way, by changing the temperature, one can change the atom density and thus control the change in refractive index. Finally, atomic vapours have the advantage of being immune to damage.

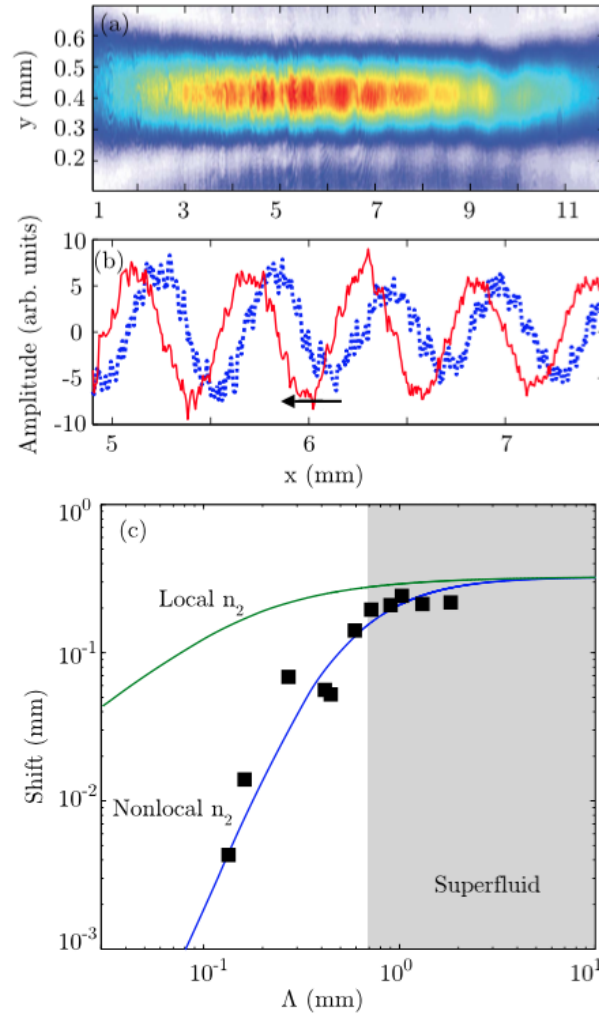


FIGURE 2.3: “(a) Raw data image of the beam at the sample output. The sound wave is barely visible due to the low (less than 10% contrast) of the modulation amplitude. (b) Amplitude profile of the sound wave after subtracting the pump beam profile for two different input pump powers: low-power measurement (dotted blue line) and high-power measurement (showing a shift in the wave, indicated by the arrow; solid red line). (c) Relative shift ΔS versus Λ : the solid green line shows the predicted shift for a local nonlinearity of $\Delta n = -7.6 \times 10^{-6}$; the corresponding healing length is $\xi = 85 \mu\text{m}$. The solid blue line includes a nonlocal nonlinearity with $\Delta n = 7.6 \times 10^{-6}$ and nonlocal length $\sigma = 110 \mu\text{m}$. The shaded gray area highlights the region in which, even in the presence of nonlocality, the medium acts as a superfluid. The black squares indicate the measured shift values at various wavelengths, several of which (i.e., for $\Lambda > 0.7$ mm) lie in the superfluid region.” [24]

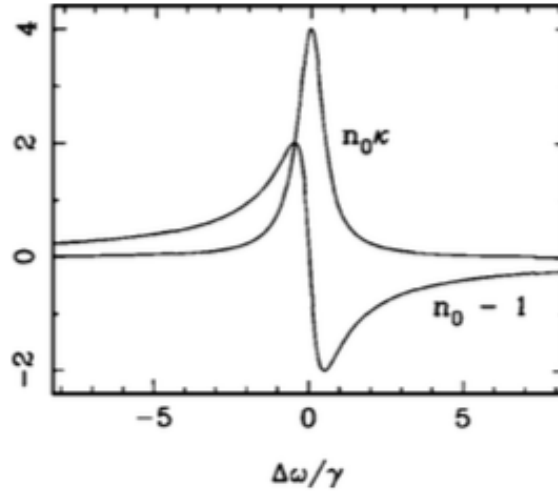


FIGURE 2.4: “Plot of the absorption n_0 and refractive index $n_0 - 1$ for an atomic gas near an atomic resonance (arbitrary units).” [26]

McCormick et al. [29] have performed measurements of the nonlinear coefficients of the rubidium D2 line. We have used their results in order to calculate the necessary input power. Indeed, it is specified in [24] that in order to access the low frequency modes, light has to propagate in the nonlinear medium for at least one oscillation period. Translating this condition for a minimum propagation distance of 10 cm, we find the condition $\Delta n \gg 4 \times 10^{-6}$. In comparison, McCormick et al. give a theoretical Kerr index $n_2 = 2.9 \times 10^{-7} \text{ cm}^2/\text{W}$ for the D2 transition of rubidium vapour at 78°C , a number density of atoms $N = 10^{18} \text{ m}^{-3}$, a dipole matrix element $\mu_{12} = 2.52 \times 10^{-19} \text{ Cm}$ and a detuning from resonance $\delta = 1.0 \text{ GHz}$. With a laser beam of 1 W and 2 mm^2 diameter, this gives $\Delta n = 1.5 \times 10^{-5}$.

2.2.2 Imaging different propagation lengths

As explained in the article of Vocke et al., the z axis maps to the time coordinate and allows to image the evolution of the of the intensity fluctuation on top of the beam. However, this technique is somehow limited by the fact that by imaging planes within the sample, one has to take into account the nonlinear effects taking place within the sample, which can alter the measured profile. What we proposed to implement was to build a sample possessing a bevelled edge. In this configuration we would image the profile of the beam at the output of the sample. This way, by translating the sample in the transverse plane, one would change the propagating length, allowing to perform the same kind of measurements, without having to image within the sample.

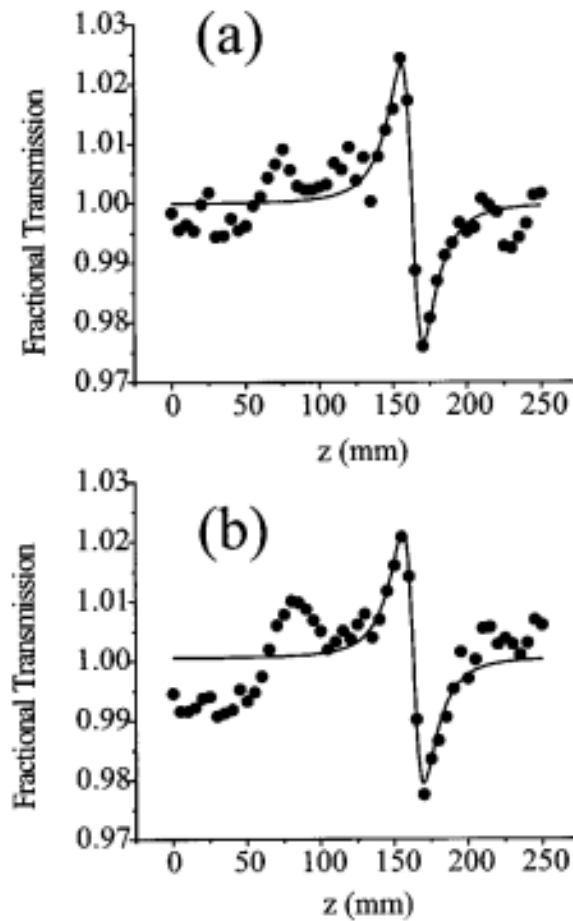


FIGURE 2.5: “Sample z scan data for scans to the red of the ^{87}Rb $F = 2 \rightarrow F'$ transition. [...] (a) [Detuning] $\delta = 0.9$ GHz, input power 6.0 mW; (b) $\delta = 1.1$ GHz, input power 8.0 mW. Fit to [theory].” [29]

2.2.3 Implementation of the experiment

As explained above, we want to use the nonlinearity of rubidium vapour to study fluids of light. This negative third order nonlinearity exists for wavelength on the red side of the Doppler-broadened absorption profile for a given transition. In order to be set at precisely the right wavelength, we use the saturated absorption peaks along with a lock-in technique to fix the wavelength. However, the saturated absorption peaks exist at the maximum of the absorption profile, which means that the absorption is maximum, which implies an unnecessary loss of power, but also a small nonlinearity. We aim at the red side of the transition to have a smaller absorption and a nonlinearity coefficient as high as possible. To this effect, the signal which we will use to lock the laser frequency will be shifted in frequency using an acousto-optic modulator. In the next sections, we will detail all the processes and tools we used to build up the experiment.

2.3 Laser source

In order to perform the measurements cited above, one needs a laser source which is both powerful and which frequency can be precisely scanned and controlled over a long range (10 GHz to cover the whole range of the D1/D2 lines of Rubidium).

2.3.1 Matisse Laser

The first laser we used was a Matisse 2 TX laser, product of the company Sirah optics. This laser is a Titanium:Sapphire ring laser which possesses an intra-cavity modulator. The operating wavelengths range from 750 to 870 nm and the scanning range exceeds 50 GHz. The pump laser used was a Verdi laser, product of the company Coherent. It could pump up to 10 W of power into the Matisse laser.

Working principle

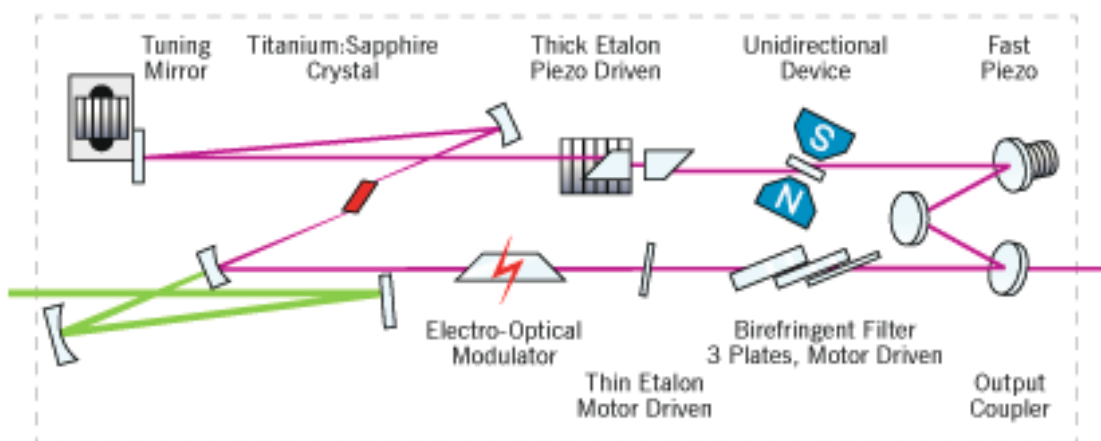


FIGURE 2.6: Optical layout of the Matisse laser. The pump beam is drawn in red, while the output beam is drawn in green. The red parallelogram is the Ti:Sa crystal. Within the cavity lie several elements which allow the operator to choose the operating wavelength as well as to perform a fine scan of the laser wavelength. Those elements are indicated on the figure and read *Tuning Mirror*, *Thick Etalon Piezo Driven*, *Unidirectional Device*, *Fast Piezo*, *Electro-Optical Modulator*, *Thin Etalon Motor Drive*, *Birefringent Filter 3 Plates, Motor Driven* and *Output Coupler*. [30]

Ti:Sa has a very large gain bandwidth. A large number of cavity modes could in principle lase for a simple cavity. In order to reach single-mode laser operation, some frequency-selective elements were added inside the cavity. Another important element of the architecture of the laser cavity is the choice of a ring cavity. With a linear configuration, the electromagnetic field is shaped as a standing wave. At the location of the nodes of the electromagnetic field, the gain cannot be depleted. Consequently, another lasing mode having its antinodes at the location of the nodes of the first mode can also oscillate

resulting in a multimode laser operation. In a ring-cavity configuration, one avoids this specific case. However, the situation one can encounter is that of two modes propagating in opposite directions, at the same frequency. In order to avoid this situation, an optical isolator is introduced in the cavity design so as to allow only one mode to oscillate in the cavity (see 2.6).

The first element of the cavity design which will select discriminate the modes is the characteristics of the optics used: the mirrors possess a very high reflectivity coating design for a specific range of wavelength. Outside of this range, the reflectivity decreases, introducing sufficient loss for the gain of the modes outside the range to be unable to reach the lasing threshold.

The second frequency selecting element is the birefringent filter, which narrows down the range of frequencies to approximately 50 GHz. It consists of three successive quartz plates of increasing thicknesses orientated at Brewster's angle. As light hits one quartz plate, the p-polarised light will suffer no reflection losses while the s-polarised light will encounter high losses. As the p-polarised light propagates through the quartz plate, its polarisation will be rotated by a certain amount which depends on the orientation of the plate's optical axis with respect to the light propagation direction, as well as the light wavelength. Hence, for a certain configuration, one quartz plate will act as a full wave plate for only a finite number of modes. The birefringent filter is tuned by rotating the quartz plates around the plates's surface normal.

The third frequency-selecting element is the thin etalon. It consists of a solid state Fabry-Pérot etalon which position is controlled by a motor. It has an FSR of about 250 GHz. In order to be sure that at least one of the laser modes is selected by it, the reflection from one face is monitored and compared to the total laser intensity, and a control loop adjusts the position of the thin etalon accordingly.

The last frequency-selecting element is the thick - piezo - etalon. It consists of two prisms forming a Fabry-Pérot cavity with an air gap. It ensures that all modes except the selected one suffer sufficiently high losses so as not to lase. The spacing of the cavity is actively controlled using a lock-in technique for the air gap to correspond to a multiple of the desire wavelength.

Alignment of the Matisse laser

The alignment of the Matisse laser, despite a rather precise procedure provided by the constructor, proved to be a very difficult and tricky exercise. The laser had been moved from a laboratory to another and thus disaligned. The numerous degrees of liberty, ranging from the position and angle of the pumping beam to the alignment of the cavity

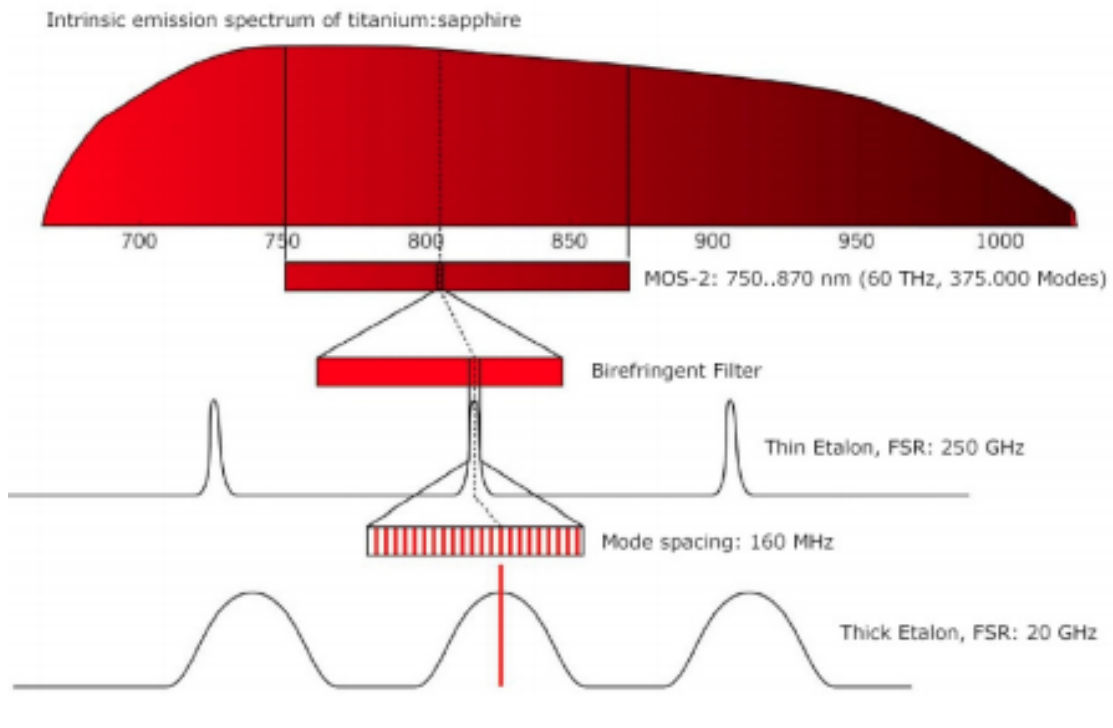


FIGURE 2.7: Frequency selection process for the Matisse laser. [30]

mirrors as well as the frequency selecting elements, made the alignment of the cavity in order to get lasing action ever so challenging.

Once laser action was reached, the optimization of the laser output was quite sensitive to the temperature variations of the room. The stability of a mode selection was thus not very good, since the natural temperature variations of the room could lead to mode hops, as well as vibrations or other events affecting the cavity stability. Another flaw of this laser was that, during frequency scans (as small as 2 GHz), we would experience mode hops. A Fabry-Pérot interferometer we constructed at the output of the laser allowed us to observe this phenomenon. This was a problem for the observation of the absorption and saturated absorption profiles of the rubidium vapour cell.

Unfortunately, the motor of the piezo etalon broke at some point after the beginning of the experiment, which forced us to switch laser since it was now impossible to precisely control the laser frequency.

2.3.2 SolsTiS® Laser

We consequently switched to a SolsTiS® laser from the company M squared lasers. This laser is an ultra narrow linewidth continuous wave Ti:Sapphire laser. It is a sealed laser, so no alignment of the cavity is required. Its performances were a good fit to

those which were required for our experiment. The physical laser was mounted on an optical table different from the one where the experiment was taking place. We thus had to transport light from one optical table to another. We did this with the help of a polarization maintaining, “APC” (Angled Physical Contact) optical fibre. We first used a “PC” fibre, but realised, by looking at the output signal, that reflections at the physical ends of the fiber lead to spurious interferences. We therefore switched to an “APC” fiber, as well as for “APC” fiber couplers. In order to have a maximum coupling efficiency, the mode size of the SolsTiS® output was matched to that of the fiber using a lens. The polarisation was also aligned with that of the fiber using the combination of a $\lambda/4$ and a $\lambda/2$ waveplate. The coupling of the light into the fiber proved to be a very difficult exercise and required much patience. However, we were able to reach a $> 80\%$ coupling efficiency. The light was thus transported to the experiment optical table. The SolsTiS® laser as well as the light coupling assembly were placed under a hood. The fans operating in it, applied a small modulation at ~ 20 Hz on the output signal. This could be suppressed by turning off the fans, but was not desirable at all times, since these fans regulate the temperature of several lasers used in the laboratory.

2.4 Saturated Absorption

2.4.1 Theory

Two-level atom model

The first model we use is that of a sample of stationary atoms which can only exist in two distinct energy level, E_1 and E_2 , and a laser field of frequency ν . The energy difference $\Delta E = E_2 - E_1$ can be translated into a frequency using Planck’s law: $\Delta E = h\nu_0$. ν_0 is the frequency of the photon associated with the transition between the two energy levels of the atom. Three different processes can change the energy state of an atom in the presence of a laser field.

Stimulated absorption is the transition between the ground and excited states of the atom, accompanied by the absorption of a photon.

Stimulated emission is the transition between the excited and ground states of the atom, accompanied by the emission of a photon, which possesses the same direction, frequency and polarization as the photons present in the laser field.

Spontaneous emission is the transition between the excited and ground states, accompanied by the emission of a photon, in a random direction with respect to the laser field.

Spontaneous emission has a rate of $\gamma = 3.810^7 \text{s}^{-1}$ [31] for the rubidium levels considered, which translates into a decay time $\Delta t = 1/\gamma = 26 \text{ns}$. In the atom's referential, photon emitted by spontaneous emission will be emitted equiprobably in all directions of space and will possess an energy spectrum with a mean value of $E = h\nu_0$ and a FWHM ΔE such that $\Delta E \Delta t = \hbar$ ie $\Delta E = \hbar\gamma$. In frequency units, the FWHM is called the *natural linewidth*: $\Gamma = \frac{\gamma}{2\pi}$. For the transition considered in rubidium atoms, $\Gamma \sim 6 \text{MHz}$.

The transition rates of the two other processes are equal and represent the probability for a ground state atom to absorb a laser photon or for an excited state atom to emit a laser photon. This rate is proportionnal to the laser field intensity (I W/cm^2), but only has a measurable effect near when $\nu \sim \nu_0$. The transition rate is αI where $\alpha = \alpha_0 \mathcal{L}(\nu, \nu_0)$ and \mathcal{L} is a Lorentzian function:

$$\mathcal{L}(\nu, \nu_0) = \frac{1}{1 + 4(\nu - \nu_0)^2/\Gamma^2}. \quad (2.4)$$

This function also describes the emission and absorption spectrum. The maximum transition rate occurs at ν_0 , and for the transitions considered, $\alpha_0 \sim 2 \cdot 10^6 \text{ m}^2/\text{J}$ [32]. The saturation intensity is defined by $I_{sat} = \gamma/\alpha_0 \sim 1.6 \text{mW/cm}^2$ for the studied transition[31]. At $\nu = \nu_0$, when $I = I_{sat}$, an excited atom has an equal probability to decay to the ground state by stimulated or spontaneous emission.

Absorption Spectroscopy

In absorption spectroscopy, a laser beam goes a cell which contains rubidium atoms, and is collected by a photodiode at the output. The laser frequency ν is scanned. Doppler shifts originates in the random thermal motion of the atoms which will have an effect on the observed profile.

As the laser beam propagates through the sample, the stimulated absorption and emission processes will modify its intensity:

$$\frac{dI}{dx} = -\kappa I \quad (2.5)$$

where

$$\kappa = h\nu n_0 \alpha (P_0 - P_1). \quad (2.6)$$

P_0 is the population in ground state, P_1 the population in excited state and n_0 the density of atoms in the sample. Without a laser field and at thermal equilibrium, the ratio of

the two atomic populations is given by the Boltzmann factor $P_1/P_0 = \exp^{-\Delta E/kT}$. At room temperature and with a weak enough laser field, $kT \sim 1/40$ eV and $h\nu_0 \sim 1,6$ eV, which means that $P_1 \ll P_0$ ie we will consider that nearly all atoms are in the ground state.

Doppler shift

Atoms in the cell are not at rest in the laboratory frame but exhibit random thermal motion. In our case, the laser beam propagation will define an axis, and to study Doppler shift, we will only need to consider the velocity component parallel to that axis: v . The density of atoms dn which has a velocity comprised between v and $v + dv$ is given by the Boltzmann velocity distribution:

$$dn = n_0 \frac{1}{\sqrt{2\pi}\sigma_v} \exp^{-v^2/2\sigma_v^2} dv \quad (2.7)$$

with $\sigma_v = \sqrt{\frac{kT}{m}}$ the standard deviation of the Gaussian distribution.

Atoms moving at v will see the laser beam frequency shifted by $\nu(\frac{v}{c})$ because of Doppler shift, which can be expressed as the fact that this population of atoms will have a shifted resonant frequency in the laboratory frame: $\nu'_0 = \nu_0(1 + \frac{v}{c})$.

The absorption coefficient of a group of atoms moving at v is thus:

$$d\kappa = h\nu\alpha_0(P_0 - P_1)\mathcal{L}(\nu, \nu'_0)dn. \quad (2.8)$$

We can define $v_{probe} = c(\nu/\nu_0 - 1)$ which is the center velocity around which the Lorentzian $\mathcal{L}(\nu, \nu'_0)$ is significantly greater than zero. The range $\Gamma' = \frac{\Gamma c}{\nu_0} \simeq 4,6$ m.s⁻¹ is significantly smaller than $\sigma_v \simeq 538$ m.s⁻¹ which means that $\exp^{-mv^2/2kT}$ remains relatively constant over Γ' . The integration of $d\kappa$ then gives $\kappa = \kappa_0 \exp^{-(\nu-\nu_0)^2/2\sigma_v^2}$, $\sigma_\nu = \nu_0\sqrt{\frac{kT}{mc^2}}$ and $\kappa_0 = n_0 h\nu\alpha_0 \sqrt{\frac{m}{2\pi kT}} \frac{c\pi\Gamma}{2\nu_0}$.

Populations As the laser beam propagates through the cell, the populations of the ground and excited states will be modified. The rate equations corresponding to this evolution are

$$\begin{aligned} \frac{dP_0}{dt} &= \gamma P_1 - \alpha I(P_0 - P_1) \\ \frac{dP_1}{dt} &= -\gamma P_1 + \alpha I(P_0 - P_1). \end{aligned} \quad (2.9)$$

The steady-state condition gives

$$P_0 - P_1 = \frac{1}{1 + 2\alpha I/\gamma}. \quad (2.10)$$

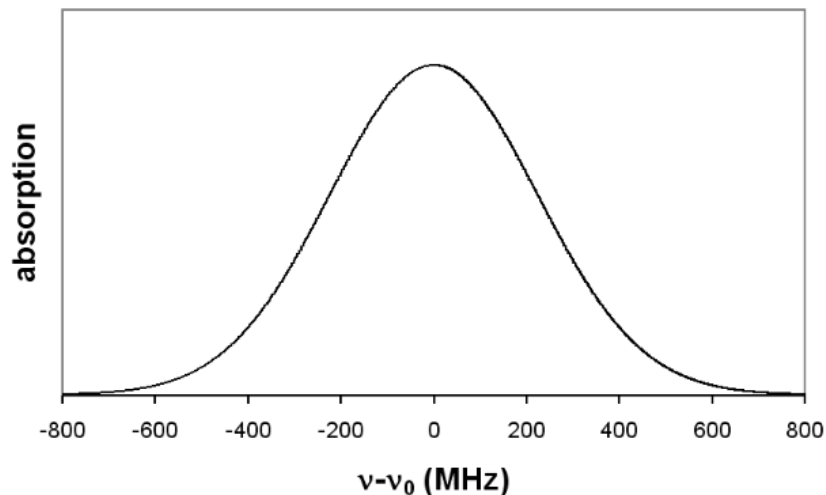


FIGURE 2.8: Absorption versus frequency detuning. The shape of the Doppler-broadened absorption profile is a Gaussian profile. Taken from [33].

This result leads to the rewriting of the expression of κ :

$$\kappa = \kappa'_0 \exp^{-(\nu-\nu_0)^2/2\sigma_\nu^2} \quad (2.11)$$

and

$$\kappa'_0 = \frac{\kappa_0}{\sqrt{1 + 2I/I_{sat}}}. \quad (2.12)$$

The width parameter σ_ν remains unchanged but the absorption coefficient is decreased to take into account the fraction of atoms which have been promoted into excited state and can no longer absorb a photon.

Saturated Absorption

In a saturated absorption experiment, the beam of a laser is divided into two unequal parts. Most of the light - typically 90 % - will constitute the *pump* beam, while the remaining part - ie. 10% - will be called the *probe* beam. Both beams come from the same laser and have the exact same frequency or intensity variation characteristics. The pump beam goes through a cell containing atoms in a vapour. The probe beam goes through this same cell, but in the other direction. We assume that the probe beam intensity is weak enough so that we can neglect its effects on the atom populations. On the other hand, the pump beam must have a strong intensity. It should promote a significant part of the atoms in the excited state so that the absorption of the beam changes as the laser frequency is scanned.

In this configuration, the probe beam will define the direction of the propagation axis. The Doppler shifted resonant frequency for an atom moving at v will consequently be $\nu_0(1 + v/c)$ for the probe beam and $\nu_0(1 - v/c)$ for the pump beam.

As seen with equation 2.8, the absorption coefficient is significantly different than zero around a frequency which is, with our new notation:

$$\nu_0'' = \nu_0 \left(1 - \frac{v}{c}\right). \quad (2.13)$$

If we define $\delta = \nu - \nu_0''$, we can rewrite equation 2.10 as:

$$P_0 - P_1 = \frac{1}{1 + \frac{2I}{I_{sat}} \mathcal{L}(\delta)}. \quad (2.14)$$

For $\delta \gg \Gamma$, we can still say that $P_0 - P_1 = 1$: the atoms are in the ground state. For $\delta = 0$, $P_0 - P_1 = \frac{1}{1 + 2I/I_{sat}}$ and for large values of I , this approaches zero. This means that the populations in excited and ground states equilibrate in presence of a strong laser field. In this situation, we say that the laser *saturates* the transition. The condition $\delta = 0$ translates into $v = v_{pump}$ where

$$v_{pump} = c \left(1 - \frac{\nu}{\nu_0}\right). \quad (2.15)$$

At a given frequency ν lying within the absorption profile, the only atoms which will experience zero detuning are those which possess a velocity near v_{pump} . $P_0 - P_1$ will be significantly different from one for these atoms only.

As seen before, the density of atoms in the ground state will follow the Maxwell-Boltzmann distribution except when $v \simeq v_{pump}$. Near this velocity, the density of ground state atoms will drop, illustrating the fact that atoms possessing this velocity are promoted to the excited state. This process is called *hole burning*.

The probe beam absorption is proportionnal to $P_0 - P_1$, which remains close to one except for $v \simeq v_{pump}$. Consequently, when $|\nu - \nu_0| \gg \Gamma$, the pump and probe beams address two different categories of atoms. On the contrary, when close to the resonant frequency ($\nu = \nu_0$ which means $v_{pump} = v_{probe} = 0$), the atoms which interact with the pump beam are the same as those which interact with the probe beam. In this situation, the frequency scan will result in a Doppler-broadened profile which features what is called a *Lamb dip* at $\nu = \nu_0$.

Multilevel effects

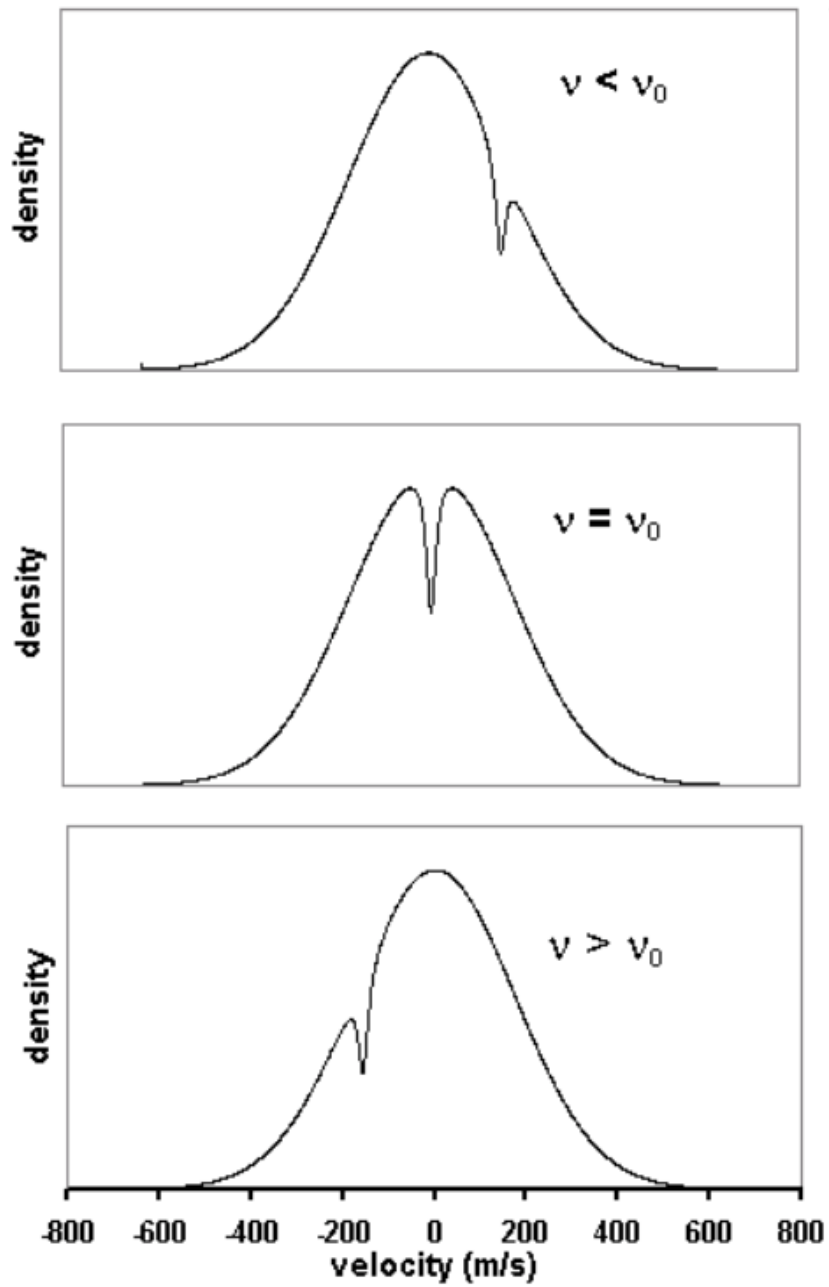


FIGURE 2.9: Density of ground state atoms versus velocity of the atoms in the lab frame. The Lamb dip appears near the velocity which Doppler shift the laser frequency to ν_0 . Taken from [33].

The two-level atom model is too simple to describe the energy levels of the rubidium atom. The description of the transitions between the different energy levels is therefore more complex.

One phenomenon which occurs is the appearance of crossover resonances, when two transitions are close enough in energy so that their Doppler-broadened profiles overlap. In this configuration, the atom possesses a single ground level and two excited states 1 and 2, resulting in two transitions of resonant frequencies ν_1 and ν_2 . We assume they are spaced less than a *Doppler width* apart. Without a pump beam on, we would observe two Doppler-broadened profiles centered on ν_1 and ν_2 . With the pump beam on, the ground state velocity profile will feature two Lamb dips as described by saturated absorption. Another dip, the *crossover-resonance dip*, arises at a frequency $\nu_{12} = \frac{\nu_1 + \nu_2}{2}$. Indeed, at this frequency, the pump and probe beam interact with two groups of atoms which have opposite velocities: $v_{\pm} = \pm c \left(\frac{\nu_2 - \nu_1}{2\nu_{12}} \right)$. Atoms at ν_+ will be resonant with one excited state while atoms at ν_- will be resonant with the other excited state. The pump beam depletes the ground state population at both these velocities which results in the “burning” of a hole at this frequency.

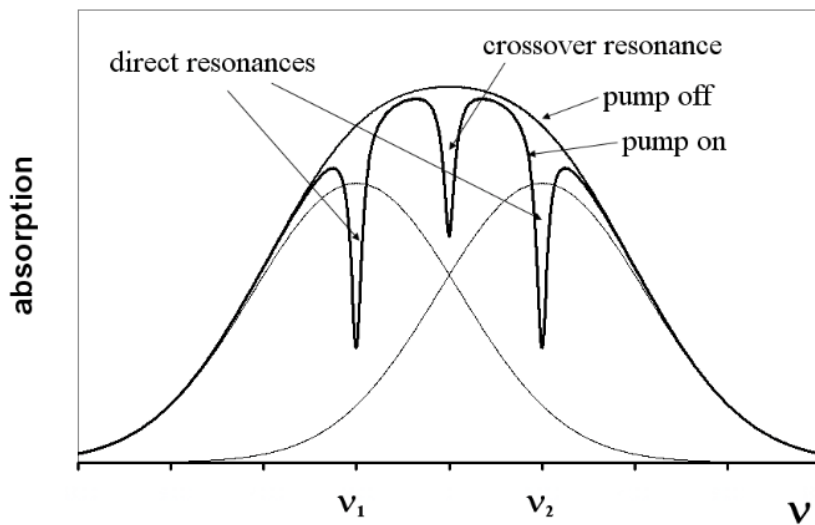


FIGURE 2.10: Absorption versus detuning in the case of a crossover resonance situation. The Doppler-broadened resonance curves of transitions at ν_1 and ν_2 are drawn as well as the sum of those two curves which corresponds to a “pump off” situation. The “pump on” curve shows the Lamb dips at ν_1 and ν_2 as well as at the crossover resonance. Taken from [32].

Another phenomenon occurring is called *optical pumping*. This phenomenon occurs when an excited state can decay into two different ground states and that these states are separated in energy by a difference greater than a Doppler width. Optical pumping occurs if the laser frequency is resonant with the transition from only one of the ground state levels but the excited state decays with equal probability to both the ground

states. In this configuration, each time an atom undergoes a transition between ground and excited state, there is a probability it will decay into the “other”, non resonant, ground state and become unable to interact with the laser field. Therefore, it can no longer play a role in the absorption process.

Energy levels of rubidium

In order to calculate the energy levels of an atom, we use the central field approximation, which is the one usually used to simply describe the energy distribution of an atom. The rubidium atom has an atomic number of 37. Using this description’s notation, its ground state configuration is $1s^2 2s^2 2p^6 3s^2 3p^6 3d^1 4s^2 4p^6 5s$: one electron is outside the inert argon core. The next higher energy configuration sees the 5s electron promoted to the 5p orbital without any change for the other 36 electrons.

The spin-orbit interaction and the Coulomb interaction are responsible for a *fine structure* of energy levels within one configuration. The Coulomb interaction accounts for the interactions between one electron and any other electron as well as with the nucleus. The spin-orbit interaction is associated with the orientation energy $-\mu \cdot \mathbf{B}$ of the internal magnetic field \mathbf{B} and the magnetic dipole moment of the electron μ . When taking these interactions into account, the energy levels of the rubidium atom can be described using the Russel-Saunders coupling scheme, which leads to the definition of new angular momentum quantum numbers.

- L is the magnitude of the total orbital angular momentum: $\mathbf{L} = \sum \mathbf{l}_i$
- S is the magnitude of the total electronic spin angular momentum: $\mathbf{S} = \sum \mathbf{s}_i$
- J is the magnitude of the total electronic angular momentum: $\mathbf{J} = \mathbf{L} + \mathbf{S}$.

Those values are indicated in the following form: $^{2S+1}L_J$. The letters S, P and D correspond to $L=0, 1$ and 2 . In the ground (5s) state configuration, the rubidium atom is described by $L=0$ and $S=1/2$, which is written as $^2S_{1/2}$. In the next (5p) configuration, $L=1$ and $S=1/2$ and $J=1/2$ or $J=3/2$. Those configurations are labelled $^2P_{1/2}$ and $^2P_{3/2}$.

Within these fine structure levels, we can again distinguish a *hyperfine structure* within which the energy difference is due to the nuclear magnetic moment in the magnetic field of the atom. \mathbf{F} , the total angular momentum describes these levels.

Rubidium naturally possesses two isotopes ^{87}Rb (72% abundant) and ^{85}Rb (28% abundant). For both isotopes, this hyperfine structure shapes two hyperfine levels within the $^2S_{1/2}$ and $^2P_{1/2}$ fine structure, and four hyperfine levels within the $^2P_{3/2}$ fine structure.

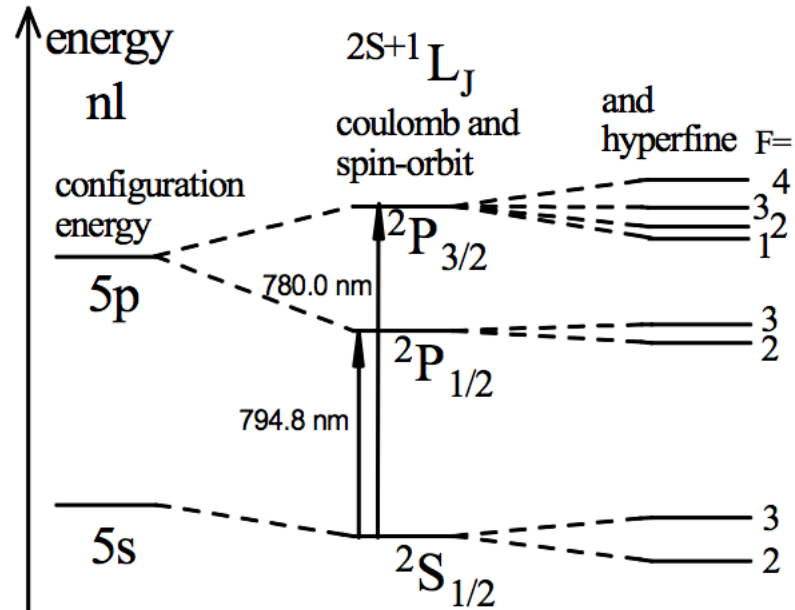


FIGURE 2.11: Energy levels in ^{87}Rb . The energy difference is not to scale. Taken from [32].

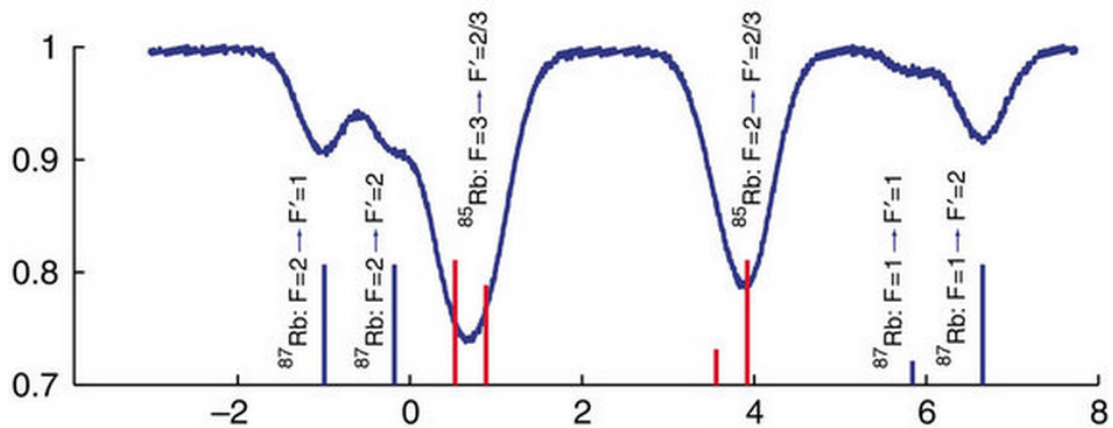


FIGURE 2.12: Light transmission versus frequency detuning. Rubidium Doppler broadened absorption spectrum, with labels for the different transitions and isotopes. Taken from [33].

2.4.2 Acousto-optic modulator

We do not want to be frequency-locked exactly on a saturated absorption peak, but at frequency shifted from this reference. We build the experiment in the following way. At the output of the fibre, a small fraction of the power is selected using a polarising beam splitter to be used in the “frequency locking” part of the experiment (see 2.13). This light then goes through a second beam splitter. The first beam which goes out is directed towards a rubidium vapour cell and is collected at the output by a photodiode. The second part goes towards an acousto-optic modulator (AOM). This AOM from 11 Opto-electronic has an optical transmission superior to 95 % and provides a ± 110 MHz frequency shift. We implemented a double pass setting, using the -1 diffracted order which means the frequency was shifted by -220 MHz. The alignment was made with the help of [34]. This frequency shifted light was then sent on a polarising beam splitter which was followed by a $\lambda/4$ waveplate, a rubidium vapour cell, a neutral density filter and a mirror. In this way, after a double pass in this arm, the light has seen its polarisation rotated by 90 degrees and is thus reflected by the cube in the orthogonal direction, where it is collected by a second photodiode.

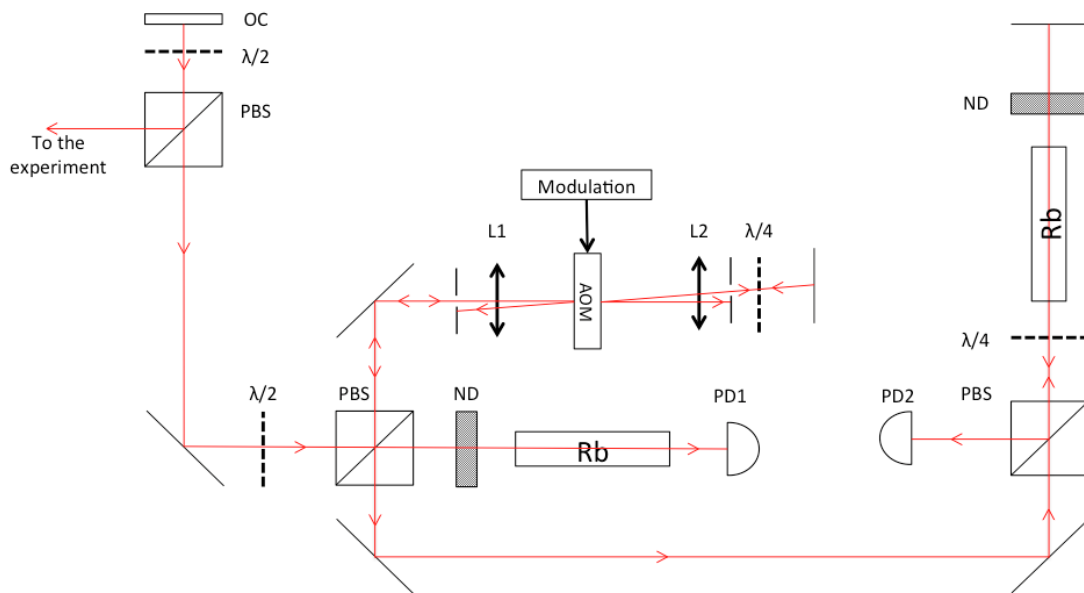


FIGURE 2.13: Layout of the frequency-locking set-up. OC: fibre output coupler, $\lambda/2$: half waveplate, PBS: polarising beam splitter, ND: neutral density filter, L1/2: lens, AOM: Acousto-optic modulator, $\lambda/4$: quarter wave plate, Rb: Rubidium cell, PD1/2: photodiode.

2.4.3 Experimental results

Figure 2.14 shows the results of a scan in frequency. The frequency is swipped over a 12.4 GHz range in 1 s.

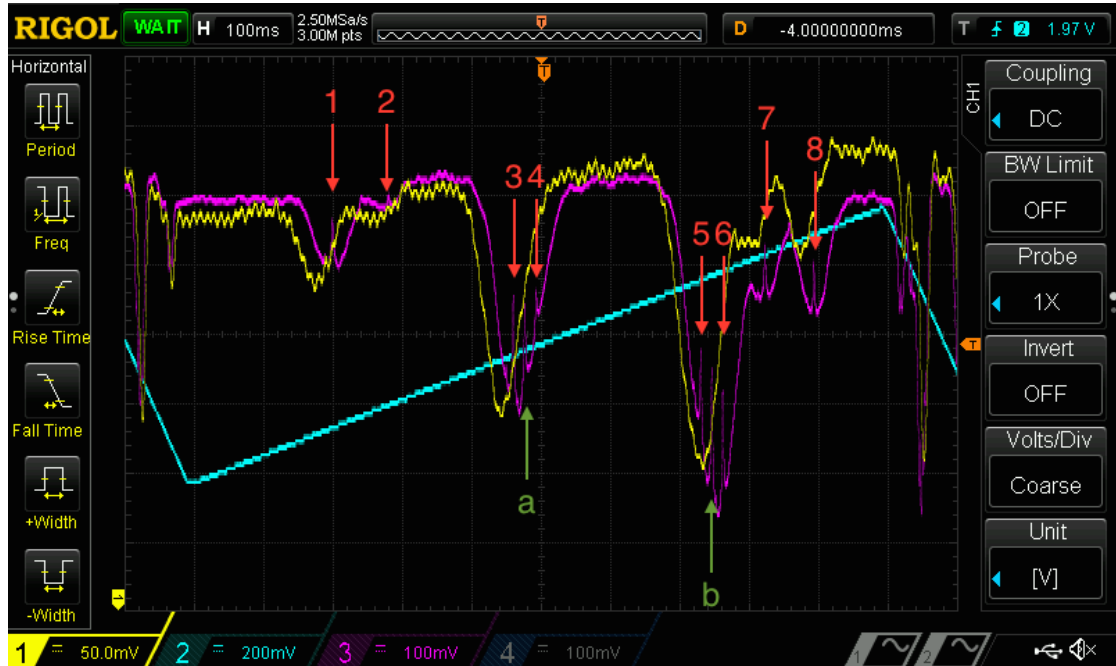


FIGURE 2.14: Impression of the oscilloscope screen. The blue curve shows the voltage ramp applied to the laser cavity in order to linearly scan the frequency. The yellow curve shows the absorption spectroscopy of a rubidium cell for the non-frequency-shifted laser beam. The pink curve shows the saturated absorption spectroscopy of a rubidium cell for the frequency-shifter laser beam. We can observe a frequency shift between the two curve which corresponds to the 220 MHz shift of the double-pass AOM. The red arrows from 1 to 8 show the saturated absorption peaks defined on 2.12. The two green arrows show two cross-over resonances.

2.5 Laser locking

In order to lock the laser to the desired frequency, we used a lock-in amplifier and a PID controller within a synchronous detection scheme.

2.5.1 Heterodyne detection

Heterodyne detection allows to extract a signal of weak amplitude but narrow bandwidth from a total signal with important noise, by multiplying the signal with a sinusoidal signal which frequency is the reference frequency. The working principle of heterodyne

detection is as follows: Let us have a signal such that $u_s(t) = U_s \sin(2\pi f_s t + \phi_s)$ and a reference signal $u_c(t) = U_c \sin(2\pi f_c t + \phi_c)$. The multiplication of the two signals gives:

$$u_s(t)u_c(t) = \frac{U_s U_c}{2} (\cos(2\pi(f_c - f_s)t + (\phi_c - \phi_s)) - \cos(2\pi(f_c + f_s)t + (\phi_c + \phi_s))) \quad (2.16)$$

The averaged value over time of this signal is zero except if $f_s = f_c$. In this case, and if the phases are matched, and the resulting signal is directly proportional to U_s .

In a more precise approach, we can see that not only is the output of the lock-in amplifier proportionnal to the modulation amplitude, but also to the derivative of the system's response. Indeed, when we modulate one physical parameter sinusoidally, the reponse of the system, recorded by the detector, may not be linear :

In our case, we modulate the laser beam frequency: $f_s(t) = \bar{f}_s + A \sin \omega t$. The detector output voltage is : $V(t) = V(f_s(t))$. This signal will be periodic in time, but not necessarily a sinusoid. The lock-in amplifier will pick-up the fundamental Fourier component of this signal and give its RMS value. However, if the amplitude of the modulation A is small enough, we can do a Taylor-series expansion of the output voltage:

$$V(t) = V(\bar{f}_s) + \left. \frac{dV}{ds} \right|_{\bar{f}_s} A \sin(\omega t) + O(A^2). \quad (2.17)$$

When running this signal through the lock-in amplifier, we get as an output:

$$U \simeq \frac{A}{\sqrt{2}} \left. \frac{dV}{ds} \right|_{\bar{f}_s}. \quad (2.18)$$

In reality, a phase difference factor between the lock-in reference and the signal must be taken into account which yields a $\cos(\theta)$, θ being the phase difference between the two signals.

Figure 2.15 shows the output signal of a lock-in amplifier for an absorption profile. This signal provides a good locking tool. Indeed, at the peak of the resonance the signal value is zero, but the derivative of the signal around this value is big, meaning that any small fluctuation around this value leads to a big signal change, which can easily be tracked and corrected by a PID controller.

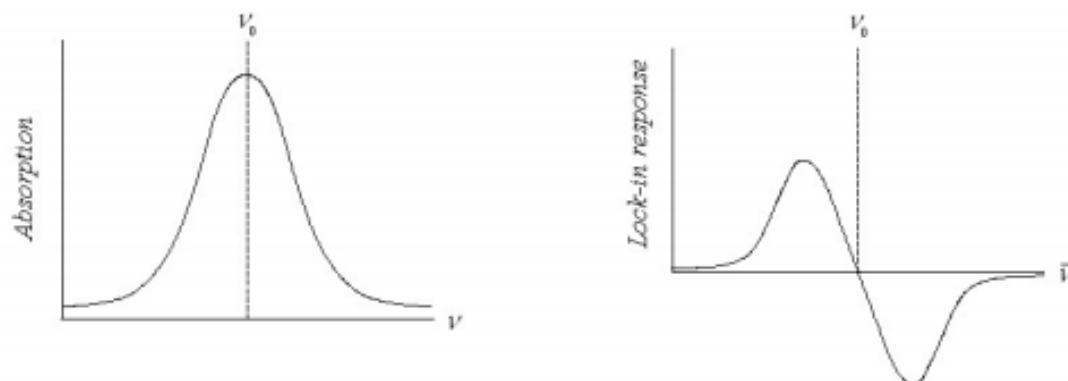


FIGURE 2.15: “Derivative of an absorption resonance.” Taken from [35].

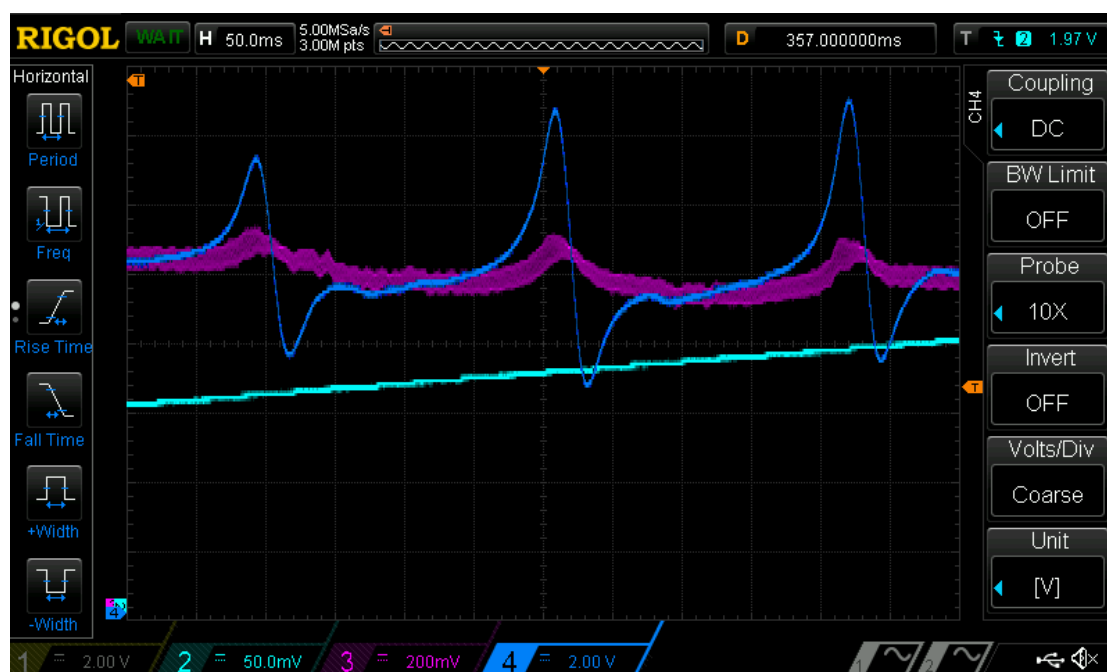


FIGURE 2.16: Impression of the oscilloscope screen. The blue curve shows the voltage ramp of the frequency scan. This scan here covers the saturated absorption peaks 3, a and 4 as labelled in 2.14. The pink curve shows the photodiode output signal: one can distinguish the frequency modulation on top of the saturated absorption signal. The blue curve shows the lock-in amplifier output signal.

Our goal was to lock ourselves on the saturated absorption peak 4 as labelled in 2.14 (transition $F = 3 \rightarrow F' = 3$ of ^{85}Rb). In order to be able to lock ourselves, we modulated the laser frequency by modulating the AOM with a reference signal at 1 kHz, which was also fed to the lock-in amplifier as its reference signal. Figure 2.16 shows, in pink, the absorption signal corresponding to peaks 3 and 4 (transitions $F = 3 \rightarrow F' = 2/3$ of ^{85}Rb) as well as their crossover resonance peak. In this figure, we can also observe, in blue, the lock-in amplifier output. The pattern from figure 2.15 is present for all three saturated absorption peaks.

2.5.2 PID controller

In order to lock the laser frequency on a saturated absorption peak, the lock-in amplifier output signal is fed to a PID controller, which in turn, feeds a correction signal to the laser cavity in order for it to stay at the desired frequency. In order to do so, we reduced the frequency scan width in order to observe only the desired saturated absorption pattern. We stopped the scanning process and turned on the PID control loop for it to bring the lock-in output signal to zero, i.e. the maximum of the saturated absorption peak. This process, while simple in theory, requires a patient setting of all the different parameters of the PID controller in order to reach a robust lock of the frequency. We managed to stay locked on the desired frequency for one hour on average. This lock was also robust to small perturbations such as small shocks.

2.6 Photon fluid experiment

Figure 2.17 presents the set-up of the experiment. Most of the light coming out of the fibre output coupler is directed by the polarising beam splitter towards the nonlinear experiment. This light is filtered by a continuously variable neutral density filter wheel. This allows to tune the power which is directed to the rubidium cell. A small portion of this beam ($\simeq 1\%$) goes towards a wavelength-meter which allows to monitor the operating wavelength. This tool is useful in order to verify the quality of the frequency-locking scheme. Most of the light is directed towards a 4-f telescope which allows to produce a collimated beam which diameter is decreased down to ~ 2 mm. The rubidium cell which follows is covered with heat stripes connected to a generator. This gives a rather fine control (down to 0.5 °C) of the cell temperature. Finally, the light is collected in a Thorlabs scanning slit optical beam profiler.

We performed beam diameter versus cell temperature measurements for the $F = 3 \rightarrow F' = 3$ transition of ^{85}Rb as well as for the crossover resonance between the $F = 3 \rightarrow$

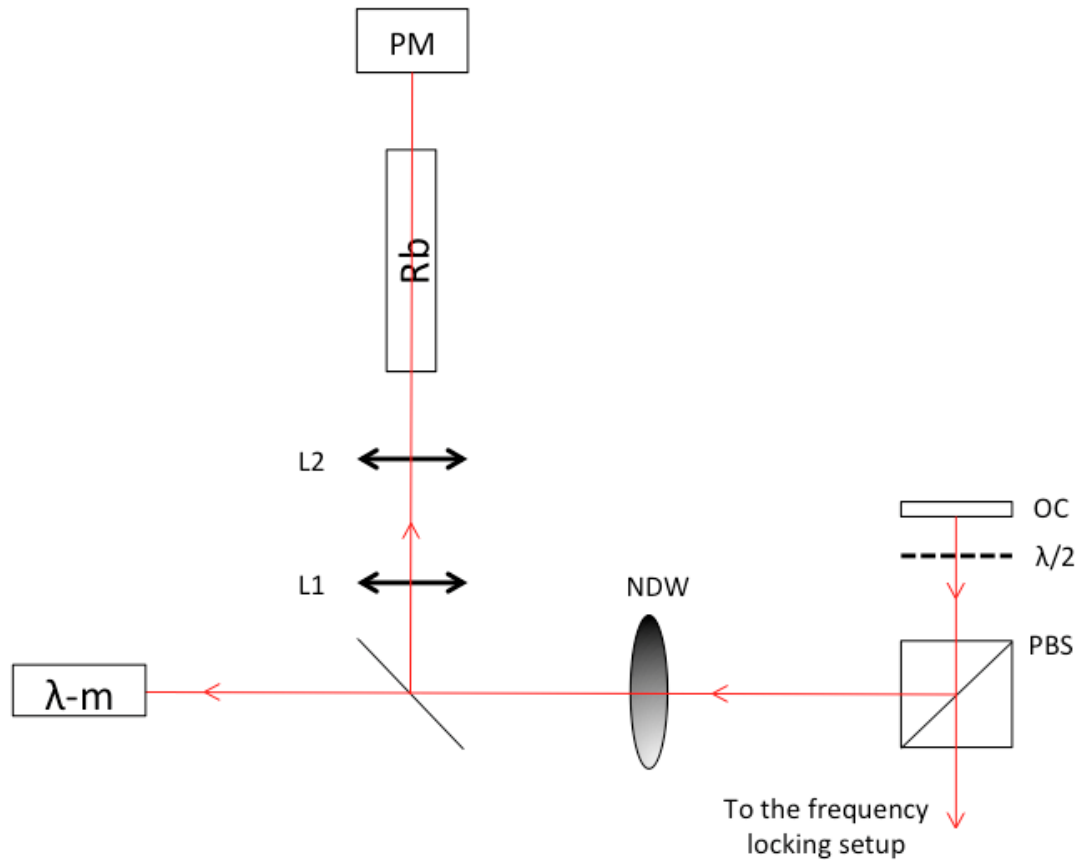


FIGURE 2.17: Layout of the nonlinear experiment set-up. OC: fibre output coupler, $\lambda/2$: half waveplate, PBS: polarising beam-splitter, NDW: continuously variable neutral density filter wheel, λ -m: wavelength meter, L1/2: lenses, Rb: rubidium vapour cell, PM: beam profiler.

$F' = 2/3$ transitions. We observed that the rise in temperature, which translates into a rise in the atomic density and thus an increase of the medium's nonlinear character, was as expected followed by an increase of the beam diameter. This confirms the negative Kerr nonlinearity of the medium.

Unfortunately, these results were obtained on the last days of my internship, and we weren't able to perform more measurements. We consequently weren't able to perform actual "photon fluid" measurements.

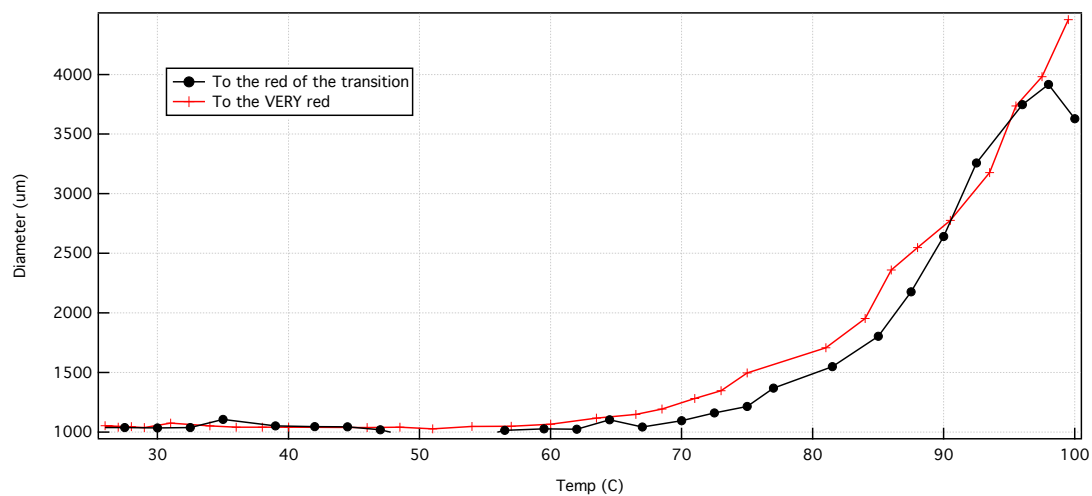


FIGURE 2.18: Beam diameter versus cell temperature. The black dots are measured for a frequency locked on the crossover resonance α . The red crosses are measured for the saturated absorption peak 4. (See 2.14.) The rubidium cell and the beam profiler are 37 cm away from each other.

Bibliography

- [1] Simon Pigeon. *Fluides Quantiques et Dispositifs à Polaritons*. PhD thesis, Mathematical Physics. Université Paris-Diderot - Paris VII, June 2011.
- [2] M. H. Anderson et al. Observation of bose-einstein condensation in a dilute atomic vapour. *Science*, 269(198), 1995.
- [3] L. P. Pitaevskii. Vortex lines in an imperfect bose gas. *Soviet Physics JETP-USSR*, 13((2)):451–454, 1961.
- [4] E. P. Gross. Hydrodynamics of a superfluid condensate. *Journal of Mathematical Physics*, 4(195), 1963.
- [5] J. F. Allen A. D. Misener. Flow of liquid helium ii. *Nature*, 141(3558):75, January 1938.
- [6] P. Kapitza. Viscosity of liquid helium below the λ -point. *Nature*, 141(3558):74, January 1938.
- [7] L. Landau. Theory of the superfluidity of helium ii. *Physical Review*, 60(4):356–358, August 1941.
- [8] Romain Hivet. *Solitons, demi-solitons et réseaux de vortex dans un fluide quantique de polaritons*. PhD thesis, Université Pierre et Marie Curie, Septembre 2013.
- [9] A. Ishikawa Y. Arakawa C. Weisbuch, N. Nishioka. Observation of the coupled exciton-photon mode splitting in a semiconductor quantum microcavity. *Physical Review Letters*, 69(23):3314, December 1992.
- [10] J. Kasprzak, M. Richard, S. Kundermann, A. Baas, P. Jeambrun, J. M. J. Keeling, F. M. Marchetti, M. H. Szymanska, R. Andre, J. L. Staehli, V. Savona, P. B. Littlewood, B. Deveaud, and Le Si Dang. Bose-einstein condensation of exciton polaritons. *Nature*, 443(7110):409–414, 09 2006. URL <http://dx.doi.org/10.1038/nature05131>.
- [11] A. Amo et al. Superfluidity of polaritons in semiconductor microcavities. *Nature Physics*, 5(805), 2009.

- [12] D. Sanvitto et al. All-optical control of the quantum flow of a polariton condensate. *Nature Photonics*, 5(610), 2011.
- [13] R. Hivet et al. Half-solitons in a polariton quantum fluid behave like magnetic monopoles. *Nature Physics*, 8(724), 2012.
- [14] A. Amo et al. Polariton superfluids reveal quantum hydrodynamical solitons. *Science*, 332(1167), 2011.
- [15] T. C. H. Liew et al. Interplay between weak localization of exciton-polaritons and the optical spin hall effect. *Phys. Rev. B*, 79(125314), 2009.
- [16] C. Leyder et al. Observation of the optical spin hall effect. *Nature Physics*, 3(628), 2007.
- [17] M. De Giorgi, D. Ballarini, E. Cancellieri, F. M. Marchetti, M. H. Szymanska, C. Tejedor, R. Cingolani, E. Giacobino, A. Bramati, G. Gigli, and D. Sanvitto. Control and ultrafast dynamics of a two-fluid polariton switch. *Phys. Rev. Lett.*, 109:266407, Dec 2012. doi: 10.1103/PhysRevLett.109.266407. URL <http://link.aps.org/doi/10.1103/PhysRevLett.109.266407>.
- [18] A. Amo et al. Exciton-polariton spin switches. *Nature Photonics*, 4(361), 2010.
- [19] C. Leyder et al. Interference of coherent polariton beams in microcavities: Polarization-controlled optical gates. *Phys. Rev. Lett.*, 99(196402), 2007.
- [20] Cristiano Ciuti Iacopo Carusotto. Quantum fluids of light. *Reviews of Modern Physics*, 85, January-March 2013.
- [21] P.-E. Larré I. Carusotto. Propagation of a quantum fluid of light in a bulk nonlinear optical medium: General theory and response to a quantum quench, .
- [22] Iacopo Carusotto. Superfluid light in bulk nonlinear media. *Proc. R. Soc. A*, 470(20140320), 2014.
- [23] P-E Larré I. Carusotto. Optomechanical signature of a frictionless flow of superfluid light, .
- [24] David Vocke, Thomas Roger, Francesco Marino, Ewan M. Wright, Iacopo Carusotto, Matteo Clerici, and Daniele Faccio. Experimental characterization of non-local photon fluids. *Optica*, 2(5):484–490, May 2015. doi: 10.1364/OPTICA.2.000484. URL <http://www.osapublishing.org/optica/abstract.cfm?URI=optica-2-5-484>.
- [25] F. Marino. Acoustic black holes in a two-dimensional photon fluid. *Phys. Rev. A*, 78(063804), 2008.

- [26] K. G. Libbrecht and M.W. Libbrecht. Interferometric measurement of the resonant absorption and refractive index of rubidium gas. *American Journal of Physics*, 74 (12):1055–1060, 2006.
- [27] J.E. Bjorkholm and A. Ashkin. cw self-focusing and self-trapping of light in sodium vapor. *Phys. Rev. Lett.*, 32(4), January 1974.
- [28] D. Grischkowsky. Self-focusing of light by potassium vapor. *Phys. Rev. Lett.*, 24: 866–869, Apr 1970. doi: 10.1103/PhysRevLett.24.866. URL <http://link.aps.org/doi/10.1103/PhysRevLett.24.866>.
- [29] C. F. McCormick, D. R. Solli, R. Y. Chiao, and J. M. Hickmann. Saturable nonlinear refraction in hot atomic vapor. *Phys. Rev. A*, 69:023804, Feb 2004. doi: 10.1103/PhysRevA.69.023804. URL <http://link.aps.org/doi/10.1103/PhysRevA.69.023804>.
- [30] Sirah. *Matisse's User Guide version 1.10*. Laser- und Plasmatechnik GmbH.
- [31] Daniel A. Steck. Rubidium 85 d line data. URL <http://steck.us/alkalidata>.
- [32] Saturated absorption spectroscopy - experiment sas. URL http://www.phys.ufl.edu/courses/phy4803L/group_III/sat_absorbtion/SatAbs.pdf.
- [33] Liron Stern, Boris Desiatov, Ilya Goykhman, and Uriel Levy. Nanoscale light-matter interactions in atomic cladding waveguides. *Nat Commun*, 4:1548, 03 2013. URL <http://dx.doi.org/10.1038/ncomms2554>.
- [34] D. J. McCarron. *A Guide to Acousto-Optic Modulators*. Durham University, <http://massey.dur.ac.uk/resources/slcornish/AOMGuide.pdf>, December 7, 2007 .
- [35] Dr. G. Bradley Armen. *Phase sensitive detection: the lock-in amplifier*. Department of Physics and Astronomy, The University of Tennessee, April 2008.